

University of Louisville

## ThinkIR: The University of Louisville's Institutional Repository

---

Electronic Theses and Dissertations

---

5-2011

### Neutral magnesium as a probe of high column density QSO absorbers.

Joseph N. Burchett  
*University of Louisville*

Follow this and additional works at: <https://ir.library.louisville.edu/etd>

---

#### Recommended Citation

Burchett, Joseph N., "Neutral magnesium as a probe of high column density QSO absorbers." (2011).  
*Electronic Theses and Dissertations*. Paper 178.  
<https://doi.org/10.18297/etd/178>

This Master's Thesis is brought to you for free and open access by ThinkIR: The University of Louisville's Institutional Repository. It has been accepted for inclusion in Electronic Theses and Dissertations by an authorized administrator of ThinkIR: The University of Louisville's Institutional Repository. This title appears here courtesy of the author, who has retained all other copyrights. For more information, please contact [thinkir@louisville.edu](mailto:thinkir@louisville.edu).

**NEUTRAL MAGNESIUM AS A PROBE OF  
HIGH COLUMN DENSITY QSO ABSORBERS**

By

Joseph N. Burchett

A Thesis  
Submitted to the Faculty of the  
College of Arts and Sciences of the University of Louisville  
In Partial Fulfillment of the Requirements  
For the Degree of

Master of Science

Department of Physics and Astronomy  
University of Louisville  
Louisville, Kentucky

May 2011



**NEUTRAL MAGNESIUM AS A PROBE OF  
HIGH COLUMN DENSITY QSO ABSORBERS**

By

Joseph N. Burchett

A thesis approved on

April 14, 2011

By the following thesis committee:

\_\_\_\_\_  
James Thomas Lauroesch

\_\_\_\_\_  
Gerard Williger

\_\_\_\_\_  
Udayan Darji

## ACKNOWLEDGEMENTS

I would like to express deep gratitude to the following individuals who have been so instrumental during my graduate career at UofL: my adviser Jim Lauroesch for being incredibly generous with his time, support, and expertise as well as counseling throughout the PhD program application process; Joe Meiring, a former postdoc at UofL who took me under his wing when I first joined our extragalactic astronomy group and continues to serve as a mentor and friend; Lutz Habertzettl, my our department research astronomer who has patiently helped me learn the “tools of the trade” and served as ex officio member of my thesis committee; and my thesis committee members Gerry Williger and Udayan Darji for their signatures...but also for Gerry being a continuous source of encouragement as well as a gifted educator, and Darji’s important perspective as a mathematician and ability to put those around him at ease (even if real mathematicians make astronomers tremble in their boots!). I am also indebted to Gary Ferland with his guidance on photoionization modeling and to Ed Jenkins for referring me to some pertinent papers on magnesium. Also, I’m not sure any of this would have taken place had it not been for Christopher Davis, the graduate program director at UofL, who not only entertained a phone call three years ago from a stranger who thought taking a quantum mechanics class might be fun, but encouraged that guy to take it a step or two

further. Lastly, I'm eternally indebted to Amanda Houpt for her love, understanding, and partnership.

## ABSTRACT

# NEUTRAL MAGNESIUM AS A PROBE OF HIGH COLUMN DENSITY QSO ABSORBERS

Joseph N. Burchett

April 14, 2011

QSOs, providing distant, luminous sources of radiation, provide a means to detect gas by absorption in the interstellar and intergalactic medium. Of particular interest to astronomers studying metal line systems in lines of sight to QSOs are the classes characterized by their neutral hydrogen column density known as Damped Lyman- $\alpha$  systems (DLAs) and Sub-damped Lyman- $\alpha$  systems (Sub-DLAs). DLAs and Sub-DLAs provide a means to probe the detailed abundance and dust content of the Universe at high redshift, revealing the evolving presence of elements heavier than hydrogen and helium. Here, we present a correlation between ionization and metallicity as indicated by the abundance ratios  $[\text{Si II} / \text{Mg I}]$  and  $[\text{Zn II} / \text{HI}]$ , respectively, in such systems at redshift  $z \sim 0.5-2.7$ . The abundances used were drawn from the literature where reported. However, where elemental abundances were omitted in the literature, we profile fit those spectra to obtain them. We believe that this correlation, if proven valid, could provide another tracer of evolution of elements throughout the history of the Universe.

## TABLE OF CONTENTS

ACKNOWLEDGEMENTS	iii
ABSTRACT	v
LIST OF FIGURES	viii
LIST OF TABLES	ix
INTRODUCTION AND BACKGROUND	1
QSO Spectral Features	3
Distant Objects as Tools to Study the Early Universe	6
Measurement of Absorption Lines	9
Nucleosynthesis and the Enrichment of the ISM/IGM	14
QSO ABSORPTION LINE SYSTEMS AND THEIR PROPERTIES	16
Dust Depletion	17
Metallicity	19
Abundance Ratios	20
DATA	24
Sources of Data	24



Profile Fitting of Archival Spectra	30
DATA ANALYSIS	39
Kendall Tau Rank Correlation Coefficient	39
Schmitt's Binned Linear Regression	43
INTERPRETATION AND CONCLUSION	45
Photoionization Models	45
Dust Shielding	47
Conclusion	50
REFERENCES	52
CURRICULUM VITAE	55

## LIST OF FIGURES

Figure 1: Absorption from gas clouds in the line of sight to a distant luminous object. . .	2
Figure 2: Sample spectrum of a QSO sight line. . . . .	4
Figure 3: Evaluation of the equivalent width. . . . .	9
Figure 4: A sample curve of growth. . . . .	12
Figure 5: Depletion patterns for several representative sight lines. . . . .	18
Figure 6: Metallicity plotted with redshift for several systems . . . . .	20
Figure 7: A trend of dust relating to systems' metallicity . . . . .	21
Figure 8: Our Data Sample . . . . .	216
Figure 9: Absorption line profile fitting for FJ0812+32. . . . .	322
Figure 10: Absorption line profile fitting for PH957. . . . .	33
Figure 11: Absorption line profile fitting for Q0841. . . . .	34
Figure 12: Absorption line profile fitting for Q1215. . . . .	35
Figure 13: Absorption line profile fitting for Q1331. . . . .	36
Figure 14: Absorption line profile fitting for Q2231. . . . .	37
Figure 15: Plot of data sample with linear regression fit. . . . .	44
Figure 16: Results of Cloudy photoionization model calculations. . . . .	466
Figure 17: Dust depletion plotted against [Si II / Mg I]. . . . .	48
Figure 18: Similar to Figure 8, but with added dimension of N(H I). . . . .	51

## LIST OF TABLES

Table 1: Lookback time and age of the Universe at various redshifts.....	8
Table 2: Wavelengths and oscillator strengths of atomic transitions. ....	10
Table 3: A Summary of sources and observations for data used.....	27
Table 4: Column densities obtained from the literature.....	29
Table 5: Column densities obtained from profile fitting .....	27
Table 6: Input table for survival analysis indicating censoring .....	42
Table 7: Data censoring specification for the STSDAS survival analysis routines.....	433

## SECTION I

### INTRODUCTION AND BACKGROUND

It is well known that the volume between stars and even between galaxies is far from empty; the interstellar medium (ISM) and intergalactic medium (IGM) are key areas of focus for astronomers studying star formation, the formation and evolution of galaxies, and cosmology. However, these regions contain gas and dust representing a diversity of composition, temperature, and bulk kinetic properties. Various techniques are employed to study the ISM/IGM, largely dependent on the phase and/or dynamics of the system under scrutiny.

For instance, radio telescopes may be used to observe interstellar carbon monoxide (CO) and other molecules which produce emission in dense regions at long wavelengths. Also, neutral hydrogen (HI) is observed at the 21cm wavelength in emission when found in warm gas regions and in absorption when in cold gas. Cold, dusty regions are best observed in the far-infrared regime where wavelengths exceed the sizes of dust grains which lead to the obscuration of “bluer”, smaller wavelength photons. In the optical and UV regimes, another technique is to derive the chemical and physical conditions (elemental abundances, density, ionization state, etc.) in individual components for gas clouds when they happen to lie in the line of sight to a more distant star or luminous object as is illustrated in Figure 1. The data presented in this study were obtained in this manner.

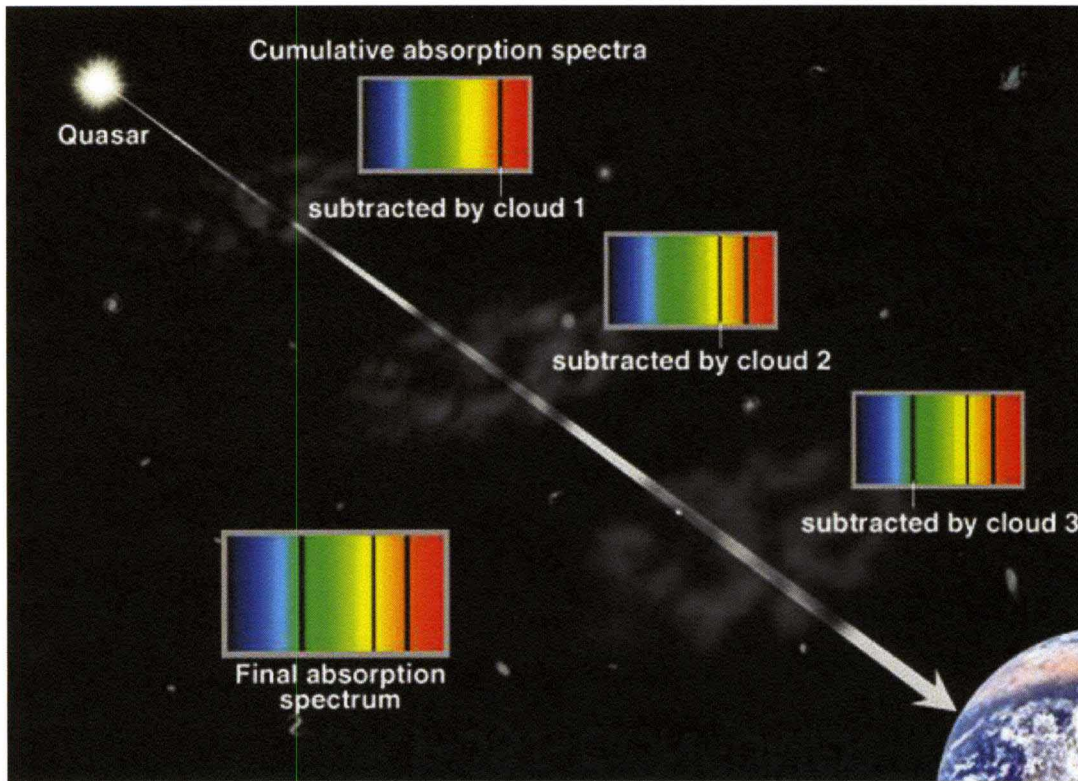


**Figure 1: Absorption from gas clouds in the line of sight to a distant luminous object. Note that the more distant objects show absorption in the redder part of the spectrum. (From Meiring, private communication)**

Photons emitted from the background radiation source are absorbed by atoms, molecules, and ions in the intervening gas, resulting in a spectrum that shows the “fingerprint” of the chemical composition of the gas. This results from photoexcitation from one quantum mechanical state to another or from photoionization where electrons in bound states are supplied with enough energy to be freed. The energy required for these transitions correspond to specific wavelengths of light by the familiar relation:

$$E = \frac{hc}{\lambda}$$

Interpretation of spectra lies at the heart of observational astronomy and the remainder of the first part of this thesis serves as an overview in relevant context and the mathematical underpinning.

### **QSO Spectral Features**

All of the sight lines for these data contain gas clouds that are seen against quasi-stellar objects (QSOs) in the background. QSOs are luminous, distant objects that emit radiation due to supermassive black holes in host *active galactic nuclei* (AGN) which constantly accrete material while also expelling material in powerful jets. The designation ‘QSO’ is used here but the term ‘quasar’ may also be encountered in similar context although a quasar is defined as being a quasi-stellar radio source (Carroll & Ostlie 2007). This ambiguity is of little consequence in this paper and is only mentioned for semantic reasons as the radio region of the electromagnetic spectrum is not used here.

Absorption lines in the continuum radiation emitted by the QSO reveal a wealth of information about the gas clouds that lie between Earth and the QSO. Figure 2 shows an example QSO spectrum which displays several characteristic properties.

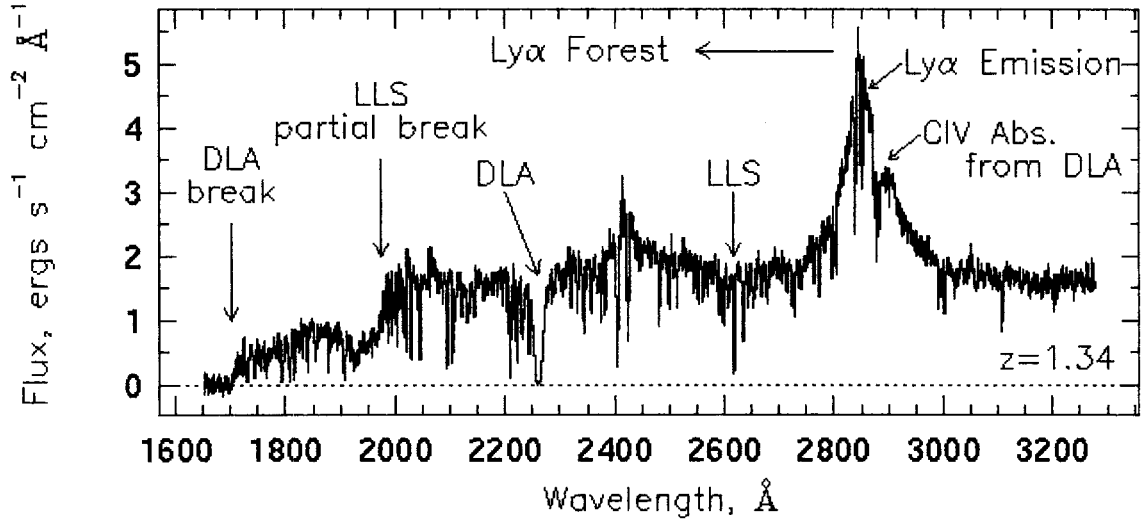


Figure 2: Sample spectrum of a QSO sight line. This particular QSO, PKS0454+039, is at a redshift of  $z=1.34$ . Two absorption systems are seen here, one of which is a damped Lyman-alpha system (Charlton & Churchill 2000).

Notice the particularly strong peak at 2850 angstroms. This peak corresponds to the Lyman- $\alpha$  ( $n=2$  to  $n=1$ ) energy transition of the hydrogen atom which has magnitude  $\Delta E = 10.2$  eV. While this transition corresponds to a wavelength of 1215.6 Å in the lab frame, the line has been *cosmologically redshifted* due to the expansion of the Universe. The relation between the transition wavelength in the lab frame to the observed (redshifted) wavelength is:

$$\lambda_{\text{obs}} = (1+z) \lambda_{\text{lab}}$$

where  $z$  is the redshift of the emitting or absorbing material. Therefore, this QSO located at a redshift of 1.34 shows the Lyman- $\alpha$  transition centered at a wavelength of 2850 Å.

The next most profound feature of this spectrum is the dense concentration of narrow absorption lines blueward of the Lyman- $\alpha$  emission peak. Known as the *Lyman- $\alpha$*

*forest*, these lines correspond to Lyman- $\alpha$  photoexcitation undergone by intervening, ionized gas clouds that exist at various redshifts between Earth and the QSO. Thus the Lyman- $\alpha$  line for each cloud is observed at a wavelength found according to  $\lambda=hc/E$  and the equivalent width of that line indicates the amount of neutral hydrogen gas contained within the cloud and its turbulent and thermal broadening, which we will explore further when we discuss measurement of absorption lines.

Abundances of interstellar and intergalactic gas are usually expressed as column densities in units of  $\text{cm}^{-2}$ . This is best visualized as a mere count of the number of atoms or molecules present in a tube with cross-sectional area 1 cm x 1 cm extending from the radiation source (star, quasar, etc.) to the observer. Generally the column density is denoted by  $N(X)$  where  $X$  specifies the atom, molecule, or ion being measured and uses spectroscopic notation to represent ionization state such as HI (neutral hydrogen), CIV (triply-ionized carbon), etc. Certain values of column density reflect unique spectral features or serve as defining criteria of intervening clouds.

One such spectral feature, the *Lyman limit* (also called the *Lyman break*), refers to the nearly complete absorption of incident radiation at wavelengths less than 912 Å in the rest frame. This wavelength corresponds to the ionization energy ( $\sim 13.6$  eV) of the hydrogen atom indicating that incident photons supply enough energy to free electrons from their bound states with host nuclei. When the column density of neutral hydrogen exceeds  $2 \times 10^{17} \text{ cm}^{-2}$ , enough atoms are present to absorb (and be ionized by) photons exceeding this energy. While the rest frame wavelength of 912 Å exists in the extreme ultraviolet regime, with increasing redshift this Lyman limit is moved to redder (longer) wavelengths, leaving the shorter wavelengths devoid of flux in the spectrum. This



creates a distinct drop-off feature in the spectrum and astronomers exploit this distinct feature using methods beyond the scope of this thesis.

### **Distant Objects as Tools to Study the Early Universe**

It was stated above that studying the intergalactic medium gives insight to the formation and evolution of galaxies and stars. Due to the finite speed of light ( $c \approx 3 \times 10^8$  m/s) and the expansion of the Universe, when we observe objects at greater and greater distances, we are peering further and further back in time. For instance, the Andromeda Galaxy (M31) is located approximately 800 kiloparsecs away (Sparke & Gallagher 2007), a distance that takes approximately 2.6 million years for light to travel. Thus, the photons that we detect today originated 2.6 million years ago. Considering that Andromeda is nearby on cosmological distance scales, objects much further away clearly provide insight into a younger Universe.

So, the redshift that causes absorption lines of certain transitions to be observed at longer wavelengths arise from the velocity at which objects are moving away from us. As Edwin Hubble was able to prove, this *recessional velocity* is directly related to the distance to these objects and the relation is known as Hubble's Law:

$$V_r \approx H_0 d$$

Where  $V_r$  is the recessional velocity,  $H_0$  is the Hubble constant, and  $d$  is the distance to the object.

Therefore, with increasing redshift we have a greater *lookback time*, or time since the observed light was emitted or absorbed. Though we omit a detailed discussion of the underlying cosmology, it is useful to have some reference for lookback times as they relate to common observable redshifts. A useful online tool for this is *Ned Wright's Javascript Cosmology Calculator*<sup>1</sup>. Several redshift values and their corresponding lookback times from this online calculator are provided in Table 1. For all these calculations, we have assumed a flat universe, Hubble constant  $H_0 = 71 \text{ km s}^{-1} \text{ Mpc}^{-1}$ ,  $\Omega_M = 0.27$ , and  $\Omega_{\text{vac}} = 0.73$ .

Also online, Wright has published the accompanying *Ned Wright's Cosmology Tutorial*<sup>2</sup> which is very useful for further explanation of basic cosmological concepts.

---

<sup>1</sup> <http://www.astro.ucla.edu/~wright/CosmoCalc.html> (Retrieved 4/1/2011)

<sup>2</sup> [http://www.astro.ucla.edu/~wright/cosmo\\_01.htm](http://www.astro.ucla.edu/~wright/cosmo_01.htm) (Retrieved 4/1/2011)

z	Lookback Time (Gyr)	Age of Universe (Gyr)
0.25	2.916	10.749
0.5	5.019	8.646
0.75	6.567	7.098
1	7.731	5.934
1.25	8.623	5.042
1.5	9.32	4.345
1.75	9.875	3.79
2	10.324	3.341
2.25	10.692	2.973
2.5	10.999	2.666
2.75	11.256	2.409
3	11.476	2.189
4	12.094	1.571
5	12.469	1.196
10	13.183	0.482
100	13.649	0.016

**Table 1: Lookback time and age of the Universe at various redshifts, assuming a flat Universe with  $H_0 = 71 \text{ km s}^{-1} \text{ Mpc}^{-1}$ ,  $\Omega_M = 0.27$ , and  $\Omega_{\text{vac}} = 0.73$  (Ned Wright's Javascript Cosmology Calculator)**

## Measurement of Absorption Lines

As stated above, absorption lines occur in a spectrum due to energy transfer from incident radiation to the absorbing material. Above, we mentioned some specific transitions associated with the hydrogen atom, but QSO absorption line spectroscopy concerns itself with any observable element. Table 2 lists several commonly seen transitions and wavelengths at which we might detect their presence by absorption.

Beyond the identity of elements present and their ionization states, we can also measure abundances of these species in absorption lines. Figure 3 shows an (highly idealized) example of an absorption line where the vertical scale is the intensity of the measured radiation and the horizontal scale, although labeled as frequency, may be interpreted as either frequency or wavelength.

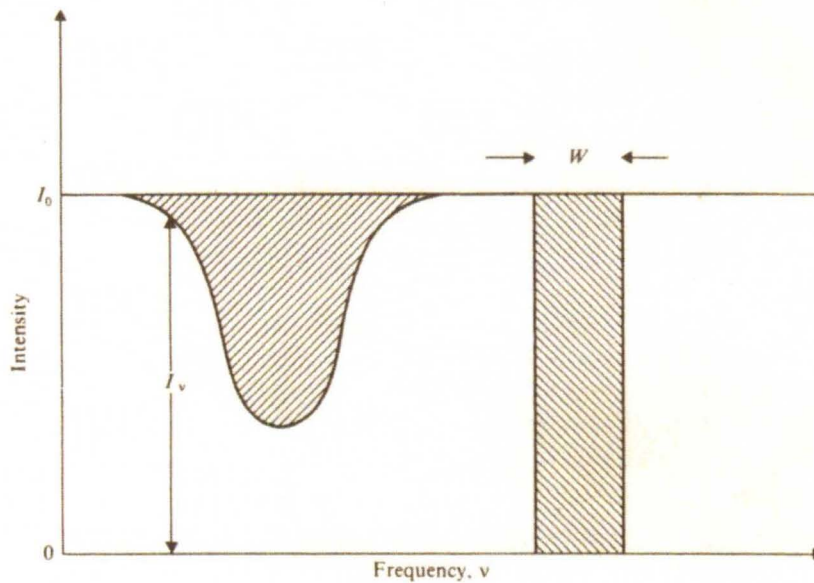


**Figure 3: Evaluation of the equivalent width. The shaded rectangle is constructed to span from the continuum to the zero-flux axis such that the two shaded areas are equal. The equivalent width is defined as the width of this rectangle.**

Element/Ion	$\lambda$ ( $\text{\AA}$ )	$f$
H I	1215.6701	0.416400
C IV	1548.1950	0.190800
	1550.7700	0.095220
Si II	1808.0130	0.002186
Zn II	2026.1360	0.489000
	2062.6640	0.256000
Mg I	2026.4768	0.113000
	2852.9642	1.810000
Cr II	2056.2539	0.105000
	2062.2340	0.078000
	2066.1610	0.051500
	2249.8768	0.001821
Fe II	2260.7805	0.002440
	2344.2140	0.114000
	2374.4612	0.031300
	2382.7650	0.320000
	2586.6500	0.069100
	2600.1729	0.239000
	2576.8770	0.350800
Mn II	2594.4990	0.271000
	2796.3520	0.612300
Mg II	2796.3543	0.615500
	2803.5310	0.305400

**Table 2: Wavelengths and oscillator strengths of atomic transitions.**

The incident radiation field on the absorbing material forms a continuum, labeled  $I_0$  on the vertical axis. In the normalization process with a real spectrum, we would fit a polynomial function to the continuum. To the right of the absorption line, we see a vertical strip constructed so that its area is equal to the shaded area of the region between the line and the continuum. Note that the height of this strip extends from the continuum to the axis of zero intensity. The strip's width is called the *equivalent width* and may be expressed mathematically by:

$$W = \int \left( 1 - \frac{I(\nu)}{I_0} \right) d\nu$$

Where  $I_0$  is the continuum radiation intensity and  $I(\nu)$  is the intensity at a given frequency (Dyson & Williams 1997). It is then useful to introduce the *optical depth*  $\tau_\nu$  which relates both the continuum intensity and the measured (absorption) intensity by<sup>3</sup>:

$$I(\nu) = I_{\nu 0} e^{-\tau_\nu}$$

The equivalent width may then be rewritten in terms of the optical depth as:

$$W = \int (1 - e^{-\tau}) d\nu$$

As we wish to ultimately derive the column density of the absorbing material, we then express the optical depth as a product of the column density  $N$  and the cross-section  $\sigma$  of absorption or scattering of the incoming photons:

$$\tau_\nu = N\sigma_\nu$$

The relationship between column density and equivalent width is then clearly dependent on the interaction cross-section of incident photons. A *curve of growth* is often used to depict this relationship such as that of Figure 4. For small  $N$ , we may use a mean cross-section over  $\Delta\nu$  to make the following approximation:

$$W = N\sigma_0\Delta\nu$$

---

<sup>3</sup> The next four equations are adapted from *The Physics of the Interstellar Medium* by Dyson & Williams (Institute of Physics Publishing 1997).

This is known as the *linear portion* of the curve of growth. When the optical depth becomes “large”, we see saturation that contains contribution from instrumental as well as kinematic effects (Welty, Hobbs, and Kulkarni 1974). Here the relationship between column density and equivalent width goes from  $W \propto N$  to  $W \propto (\ln N)^{1/2}$ . We call this the *flat portion* of the curve of growth, where the column density and equivalent width have a much weaker dependence on one another. By further increasing the column density (and thus the optical depth), we begin to see damping wings in the absorption line and the curve of growth enters the *square root portion*, so-called because  $W \propto N^{1/2}$ . In this region, the uncertainty of the measured column density dramatically decreases.

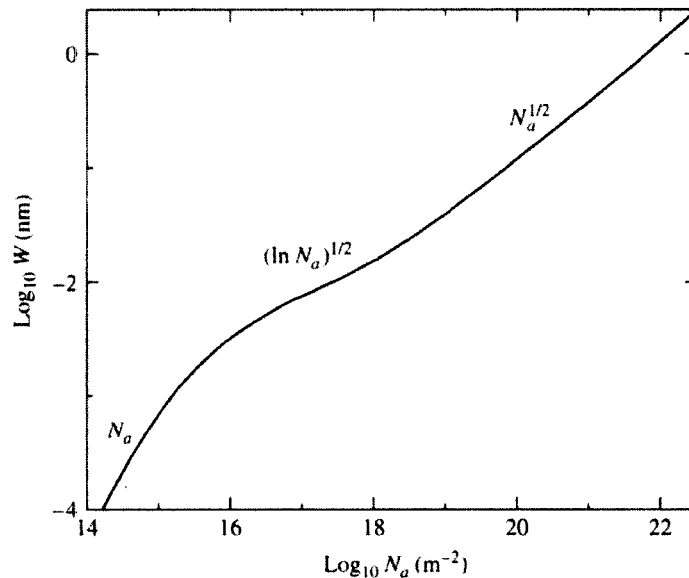


**Figure 4: A sample curve of growth. With increasing column density (and therefore equivalent width), we encounter the linear portion (unsaturated spectral line), the flat portion (saturated line but not possessing damping wings), then the square root portion (the line is so saturated that damping wings form). (Carroll & Ostlie 2007)**

While the preceding discussion focused on the relationship between column density and equivalent width, we now turn to the factors influencing the absorption cross-section  $\sigma_\nu$ . Interpreting the cross-section as the likelihood of an interaction, certain transitions between quantum-mechanical states are more likely than others. We quantify this likelihood by the oscillator strength  $f$ . For instance, the Lyman- $\alpha$  transition of the neutral hydrogen atom has an  $f$ -value of 0.4164 whereas the Lyman- $\beta$  has  $f = 0.07914$  [Morton 2004]. Therefore, the Lyman- $\alpha$  absorption is about 5.26 times more likely to occur. For a given column density of HI, the equivalent width of the Lyman- $\alpha$  line will then be correspondingly greater. Several transitions, wavelengths, and oscillator strengths are given in Table 2.

Also contributing to the shape and size of the absorption line are physical processes that have a broadening effect<sup>4</sup>. The first contribution is from *natural broadening*, resulting from the Heisenberg uncertainty principle. An infinitely sharp line would imply a zero uncertainty of the wavelength (and thus energy) measurement due to a state transition, however the brief time that an electron occupies the excited state places a nonzero lower bound on the uncertainty. A second contribution comes from the interactions that the constituent particles of the gas undergo with one another, called *pressure broadening*. Together with natural broadening, this generates a *Lorentz profile*, which mathematically takes the form:

---

<sup>4</sup> This section is paraphrased from section 9.5 of *An Introduction to Modern Astrophysics* by Bradley W. Carroll and Dale Ostlie which in itself is marginally more mathematically rigorous. For a more complete discussion of line profiles, the reader is referred to (Spitzer 1978)



$$\Delta\lambda \approx \frac{\lambda^2}{c} \frac{n\sigma}{\pi} \sqrt{\frac{2kT}{m}}$$

The third contribution is from *thermal broadening* where we take into effect Doppler shifts due to the random motions of individual particles. Clearly, these motions are due to the thermal kinetic energy possessed by the gas and are heavily dependent on its temperature. Assuming that the gas particles are distributed as a Maxwell-Boltzmann function, the width of the line at half its maximum depth due to thermal broadening will exhibit a Gaussian profile:

$$(\Delta\lambda)_{FWHM} = \frac{2\lambda}{c} \sqrt{\left(\frac{2kT}{m} + v_{turb}^2\right) \ln 2}$$

The combined effects of these broadening mechanisms can be modeled by a convolution of the Lorentz and Gaussian profiles, known as a Voigt profile. By fitting a Voigt profile to an absorption line, we may then extract these physical parameters which give rise to its size and shape.

### **Nucleosynthesis and the Enrichment of the ISM/IGM**

While the elements hydrogen, helium, lithium, and beryllium were created in the Big Bang, all elements that are heavier (atomic number > 4) are created in the inner recesses of stars. These elements are produced by the very fusion processes that generate stars' energy. Then, depending on a star's mass (and therefore ultimate fate), various mechanisms inject the surrounding space with these metals where they may become part of new stars, continuing the cycle.

Elements are generally classified according to the processes by which they are created. One classification is known as the alpha-process, so-called due to their formation which involves the continual fusion of  ${}^4_2\text{He}$  nuclei ( $\alpha$ -particles). As such, the  $\alpha$ -elements (O, Ne, Mg, Si, S, Ar, Ca and Ti) possess nuclei with even-numbers of protons. They are expelled to the ISM during Type II supernovae.

Another class of elements, called the *iron-peak* nuclei are bound together relatively tightly compared to other nuclei of similar masses. The name for this classification comes from the peak that occurs in binding energy per nucleon plotted against increasing atomic mass number. The ISM is enriched by the Fe-peak elements (Zn, Cr, Mn, Fe, Co and Ni) largely via Type Ia supernovae, although there is a lesser contribution from Type II SNe.

## SECTION II

### QSO ABSORPTION LINE SYSTEMS AND THEIR PROPERTIES

As stated in the title, this work is concerned with high column density absorption systems. The column density in question is that of neutral hydrogen, in particular where  $\log N(\text{HI}) \geq 19.0$ . The highest column systems of interest are those where  $\log N(\text{HI}) \geq 20.3$  and are known as Damped Lyman- $\alpha$  Systems or DLAs. As the name suggests, these systems have such a high column density as to show damping wings in the Lyman- $\alpha$  absorption line which exists in the rest frame at 1215.6 Å.

A second class of systems have lower column density:  $19.0 \leq \log N(\text{HI}) \leq 20.3$  and are known as sub-Damped Lyman- $\alpha$  Systems (Sub-DLAs). Here, the difference in naming is purely historical as the damping wings which characterize the DLAs are still visible in these systems but were not able to be seen in the initial low spectral resolution surveys of QSOs. As we will see in greater detail, many of these systems appear to be metal-rich. Therefore, they provide important clues into the nucleosynthetic history of the Universe (Kulkarni, et al. 2007), i.e. how the amount of metals present in stars, galaxies, and the ISM/IGM has evolved over cosmic time.

Not only is most of the hydrogen gas in DLAs and Sub-DLAs neutral, but these systems are believed to possess most of the neutral gas in the Universe (Storrie-Lombardi & Wolfe 2000, Wolfe 1995). These neutral gas clouds are the progenitors of molecular

clouds when they give way to star formation. It can be shown that DLAs and Sub-DLAs observed at earlier epochs contain enough neutral hydrogen to form all of the stars that we see today.

## **Dust Depletion**

By using the absorption line method of measuring interstellar and intergalactic abundances, we concede that the resulting column densities are only a measure of these species in the *gas-phase*. However, depending on the environment (temperature and pressure) of the gas cloud and the amount present of an element or molecule, a fair amount of material may be condensed onto dust grains. Of course, measurements of the gas-phase will underreport the total amount present if some of the species is present in the form of dust. We refer to this as *depletion*.

The tendency of some atoms and molecules to be incorporated into dust grains is greater than for others. Depletions of these so-called *refractory elements* have been studied in various environments within our Galaxy and beyond (Jenkins 2009, Savage & Sembach 1996, Cartledge et al. 2006, Welty et al. 2001) and several depletion patterns are shown in Figure 5, reproduced here from Meiring et al. (2009).

Of greatest consequence to this thesis is the considerably increased depletion of Cr and Fe relative to Zn. We discuss the specifics of these consequences later in our use of observables to trace physical conditions of absorption systems.

It should be noted that the understanding of dust content is not merely to account for inaccuracies in measured abundances; dust grains play many important roles in the ISM/IGM. In the introduction, we presented an example of observing dust-obscured environments and the fact that short wavelengths are scattered by the dust grains. This has an effect on the radiation field in a gas cloud as well since energetic UV photons may be absorbed or scattered by the grains which then reradiate at longer wavelengths. Also, dust grains happen to be the sites of molecular hydrogen formation (Hollenbach & Salpeter 1971). Stars form by the collapse of molecular clouds, therefore dust has large implications in the realm of star formation.

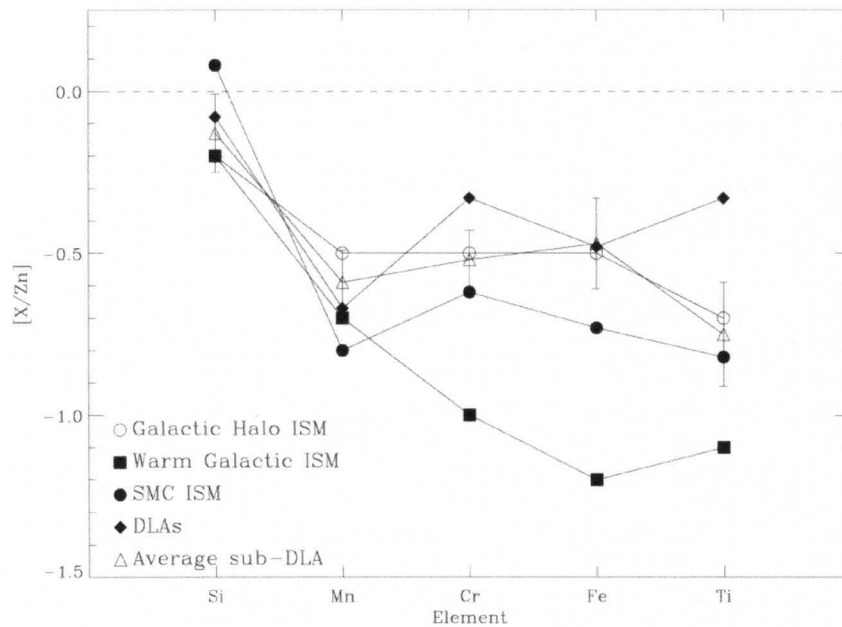


**Figure 5: Depletion patterns for several representative sight lines. Notice the small amount of depletion of Zn compared with Fe. (Meiring et al. 2009)**

## Metallicity

DLAs and Sub-DLAs offer a unique perspective into the chemical evolution of the Universe by probing the composition of dense clouds at various epochs. Of particular interest are how elements heavier than helium, the ‘metals’, came to be formed and distribute over cosmic time. We stated above that Sub-DLAs tend to be more metal-rich than DLAs, but let us now examine in greater detail the metal content of high-column absorbers, discussing means of measurement and some key observed trends.

In referring to the metallicity of a system, we shall use the relative abundance of zinc to hydrogen,  $[Zn/H]$ . This may call into question why we do not use iron, chromium, or another metal. Going back to the discussion of dust, we see a clear difference of depletion in the abundances of zinc, which has little to no depletion depending on the sight line, and these other aforementioned elements. Therefore, our measurement of zinc in the gas-phase is likely to represent a much more accurate measure of the total zinc in the system than a measurement of iron to its true abundance. Furthermore, Zn belongs to a set of elements known as the *iron-peak* elements and therefore traces very well the abundances of Fe, Cr, Ni, and others (Lauroesch et al. 1996).

As a picture of the evolving metal content in DLAs and Sub-DLAs, Figure 6 shows a plot of metallicity versus redshift reproduced from Wolfe, Gawiser, and Prochaska (2005). We see a clear increase in metallicity over cosmic time which is expected due to the cumulative enrichment of heavy elements into the ISM/IGM via supernova and stellar wind activity.

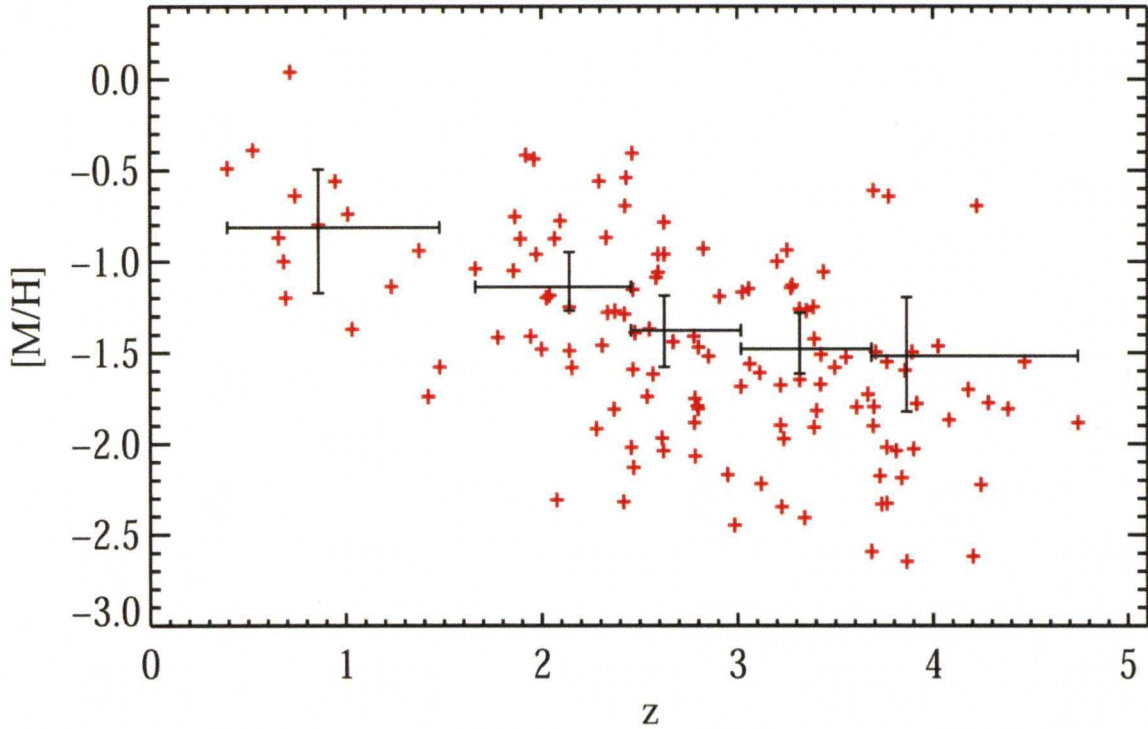


Figure 6: Metallicity plotted with redshift for several systems compiled from Prochaska et al. (2003), Kulkarni et al. (2005), and Rao et al. (2005). Overplotted are weighted mean metallicities. This figure appears in Wolfe, Gawiser, and Prochaska (2005).

### Abundance Ratios

In studying the physical characteristics of DLAs and Sub-DLAs, we use a variety of *abundance ratios*. First, to define the nomenclature (Lauroesch et al. 1996):

$$[X/Y] = \log N(X) - \log N(Y) - [X/Y]_{\text{solar}}$$

Where  $N(X)$  and  $N(Y)$  correspond to the column density of each respective element.

Essentially, we are expressing the abundance of one element relative to another with that ratio relative to the same elements' abundance ratio in the neighborhood of the Sun. As an example, a measurement of a system with  $[Zn/H] = -2$  tell us that the system has

1/100<sup>th</sup> the amount of zinc as hydrogen when compared with the same ratio as measured near the Sun.

In general, we use abundance ratios in attempts to derive physical characteristics of distant environments. In doing so, we must take into consideration the chosen elements' nucleosynthetic origins to insure that their comparison is meaningful (Lauroesch 1996, Timmes et al. 1996). This same reasoning was used above in stating that  $[Zn/H]$  would trace intrinsic (undepleted) values of  $[Fe/H]$  as a measure of metallicity (both are Fe-peak elements). As such,  $[Zn/Fe]$  may be used as an indication of dust content due to the greater depletion of Fe than that of Zn. An interesting trend is shown in Figure 7 where we see increasing dust content when plotted against metallicity. Again, this figure was originally provided in the review by Wolfe, Gawiser, and Prochaska (2005).

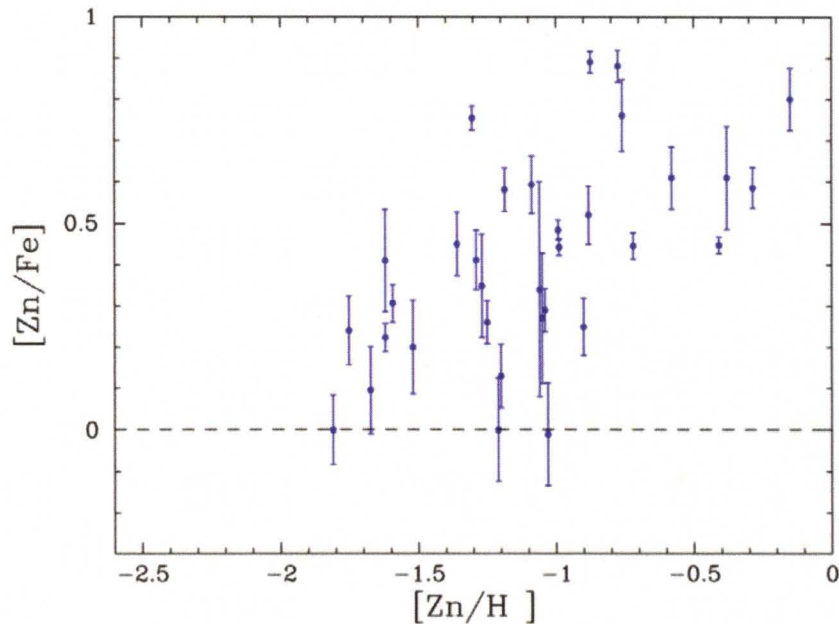


Figure 7: A trend of dust relating to systems' metallicity.  $[Zn/Fe]$  serves a tracer for dust content due to the high depletion of Fe while Zn remains largely undepleted.



Also, due to the high depletion of Cr,  $[\text{Cr}/\text{Zn}]$  similarly provides an indication of dust content as Cr is also an Fe-peak element. Referring back to figure 4, we see that through most of the sight lines Cr and Fe display comparable depletion.

Often times, ISM/IGM constituents exist in a predominately ionized state. Measuring the extent of this ionization reveals much about incident radiation upon the system and the recombination processes that may be taking place. We use  $[\text{Si II} / \text{Mg I}]$  for this study, the relative abundance of singly ionized silicon to neutral magnesium. The choice of Si II instead of Mg II is largely due to practical concerns as the lines used to measure Mg II at wavelengths  $2803 \text{ \AA}$  ( $f = 0.306$ ) and  $2795 \text{ \AA}$  ( $f = 0.616$ ) are generally too saturated to obtain accurate abundance measurements. In general, the  $\lambda 1808$  ( $f = 0.0022$ ) line of Si II is unsaturated and thus far more measurable (oscillator strength values obtained from Morton 2004 and Prochaska et al. 2003). Note that Si and Mg are also both  $\alpha$ -elements thus their presence results from Type II SNe enrichment.

We now conclude this section with a brief mention of some other abundance ratios and their corresponding physical implications. The first is  $[\alpha / \text{Fe}]$ , which is the relative abundance of the alpha-process elements (O, Ne, Mg, Si, S, Ar, Ca, Ti) to iron. As described in §1.3, the ISM is enriched with the  $\alpha$ -elements via Type II supernovae. While this clearly provides insight to history of star formation and death, work has also been done to include these data as parameters in models of galaxy evolution especially in the realm of dwarf spheroidal galaxies (Tolstoy & Venn 2003, Cohen & Huang 2010, Lauroesch et al. 1996).

Another useful abundance ratio is that of  $[N / \alpha]$ , which has been used as a tracer of a system's age. Timmes et al. (1997) as well as Pettini, Lipman, & Hunstead (1995) suggested the use of nitrogen abundances to study age-metallicity relationships. Large  $[N / \alpha]$  have been thought to be older systems since there is a predicted lag between the enrichment of  $\alpha$ -elements into the ISM (Type II SNe) and the infusion of nitrogen from stars on the asymptotic giant branch. This simple model is complicated however by further work (Prochaska et al. 2002) implying that the time separation between  $\alpha$ -enrichment and N-enrichment may not consistently result in increasing  $[N / \alpha]$  with age.

## SECTION III

### DATA

Here we present our data sample. The sample includes 30 systems (15 DLAs and 15 Sub-DLAs), all of which had previously published abundances for H I, Zn II, and Si II. However, six of the systems did not have published abundances for Mg I, which we obtained by profile fitting using publically available spectra. More detail on these data sources will be given below as will discussion of the profile fitting procedure. Visual comparison of the abundance ratios [Si II / Mg I] and [Zn II / H I] appeared to suggest a correlation<sup>5</sup> which we then tested and fit using survival analysis techniques. The results of our data analysis are presented in the next section and we save the discussion of potential causes of our results for the final section of this thesis.

#### Sources of Data

The objects in our sample are derived from observations published in ten different sources: Lopez et al. (1999), Srianand & Petitjean (1998), Prochaska & Wolfe (1999), Khare et al. (2004), Prochaska et al. (2007), Meiring et al. (2007), Peroux et al. (2002), Meiring et al. (2009), Meiring et al. (2010), and Noterdaeme (2010). While adequate

---

<sup>5</sup> See figure 8

detail is given in each of these papers about their respective observations, we summarize the telescope and instrument used for the observations in Table 3.

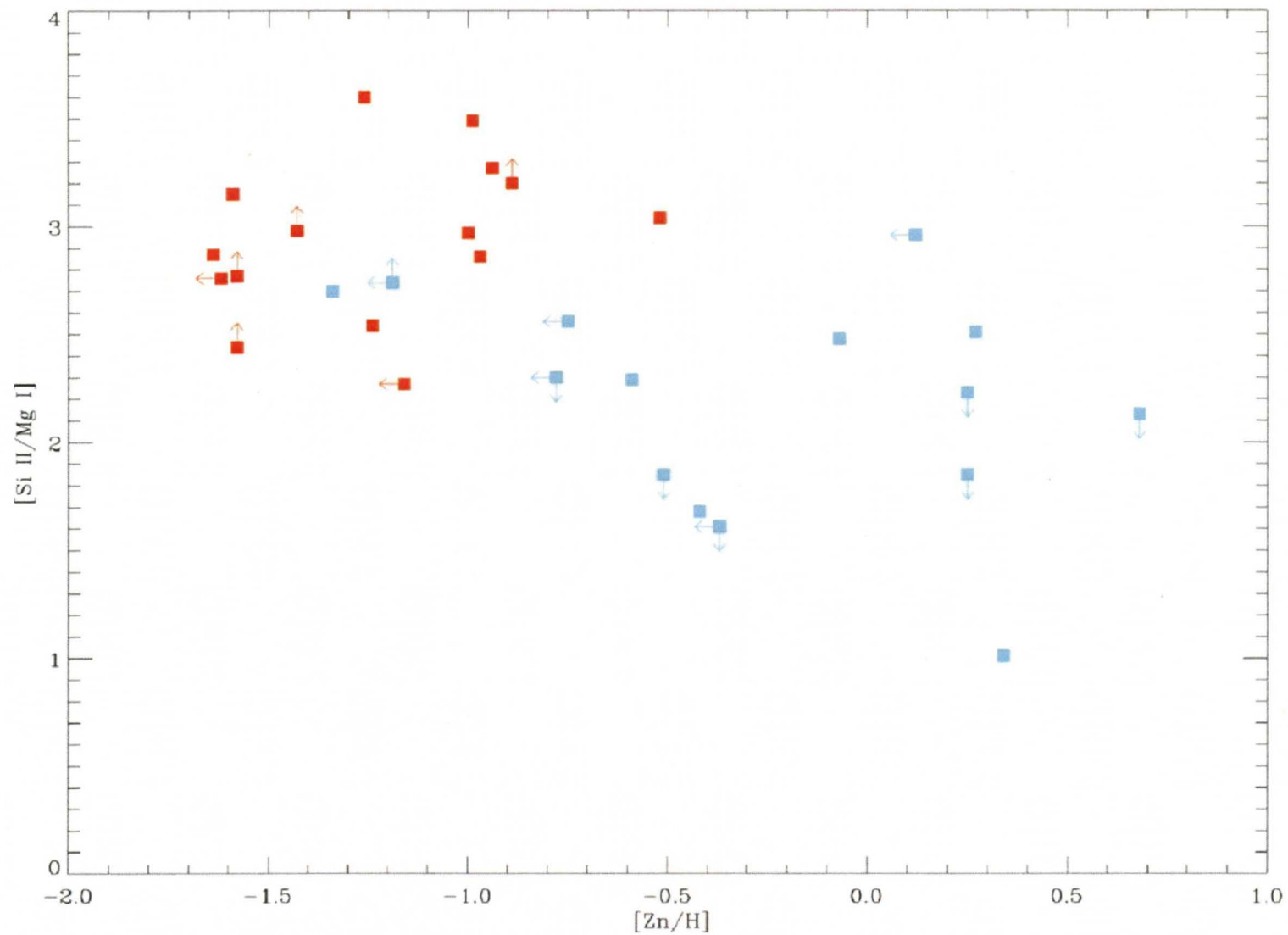


Figure 8: Our data sample. If viewed in color, the red points indicate a DLA where the blue points represent Sub-DLAs.

QSO	z	Paper	Telescope	Instrument
Q0826-2230	0.9110	Meiring 2007	Magellan Clay	MIKE
Q1009-0026	0.8866	Meiring 2007	Magellan Clay	MIKE
Q1010-0047	1.3270	Meiring 2007	Magellan Clay	MIKE
Q1224+0037	1.2346	Meiring 2007	Magellan Clay	MIKE
Q1224+0037	1.2665	Meiring 2007	Magellan Clay	MIKE
Q2331+0038	1.1414	Meiring 2007	Magellan Clay	MIKE
Q0933+733	1.4790	Khare 2004	MMT	Blue Channel Spectrograph
SDSS J1028-0100	0.6321	Khare 2004	MMT	Blue Channel Spectrograph
SDSS J1028-0100	0.7088	Khare 2004	MMT	Blue Channel Spectrograph
SDSS J172+5302	0.9449	Khare 2004	MMT	Blue Channel Spectrograph
SDSS J172+5302	1.0311	Khare 2004	MMT	Blue Channel Spectrograph
SDSS J2340-0053	1.3606	Khare 2004	MMT	Blue Channel Spectrograph
HE 1104-1805 A	1.6616	Lopez 1999	HST, New Technology, Keck	FOS, Multi Mode Instrument, HIRES
Q0138-0005	0.7821	Peroux 2002	VLT	UVES
Q0153+0009	0.7714	Peroux 2002	VLT	UVES
Q0449-1645	1.0072	Peroux 2002	VLT	UVES
PKS 0528-250	2.8112	Srianand 1998	La Silla 3.6m	CASPEC
Q0240-2309	1.6718	Meiring 2010	VLT	UVES
Q0012-0122	1.3862	Meiring 2009A	Magellan Clay	MIKE
Q0021+0104A	1.3259	Meiring 2009A	Magellan Clay	MIKE
Q0021+0104B	1.5756	Meiring 2009A	Magellan Clay	MIKE
Q2051+1950	1.1157	Meiring 2009A	Magellan Clay	MIKE
Q2352-0028B	1.0318	Meiring 2009A	Magellan Clay	MIKE
FJ0812+32	2.6263	Prochaska 2007	Magellan Clay	MIKE
PH957(Q0100+13)	2.3090	Prochaska 1999	W.M. Keck	HIRES
Q0841+12	2.3750	Prochaska 1999	W.M. Keck	HIRES
J1237+0647	2.6896	Noterdaeme 2010	VLT	UVES, X-shooter
Q1215+33	1.9990	Prochaska 1999	W.M. Keck	HIRES
Q1331+17	1.7760	Prochaska 1999	W.M. Keck	HIRES
Q2231-00	2.0660	Prochaska 1999	W.M. Keck	HIRES

**Table 3: A summary of objects used in this study, including objects for which profile fitting was performed and those found the literature.**

Historically, suspected DLAs were chosen to observe more closely with high resolution spectrographs due to profound absorption features seen in low-resolution spectra as part of larger surveys. For instance, the SDSS has surveyed 25% of the sky visible from Earth. However, the spectral resolution is far too low to detect many of the weaker metal lines that are of interest for in-depth abundance studies, the MgII doublet at  $\lambda\lambda$  2795, 2803 Å is so prominent as to indicate the presence of a high column density system (Lauroesch, private communication). The observed wavelengths of these lines indicate the redshift at which the responsible absorber might lie. As an example, this doublet observed at  $\lambda\lambda$  4611, 4625 Å would suggest the possibility of a system at  $z = .65$ :

$$z = \frac{4625}{2803} - 1 = 0.65$$

It should also be noted that, at such moderate redshifts, these lines fall conveniently in the optical range of the spectrum which is observable from ground-based instruments. In the rest frame, they fall in the UV which is shielded by Earth's atmosphere.

Of these 30 objects, 24 had previously published abundances that were necessary for this study. These are listed in Table 4.

QSO	z	H I	Mg I	Si II	Zn II	Cr II	Paper
Q0826-2230	0.9110	19.04 ± .04	12.09 ± 0.03	<14.22	12.35 ± 0.07	<12.11	Meiring 2007
Q1009-0026	0.8866	19.48 ± .05	12.41 ± 0.04	<14.26	12.36 ± 0.04	<12.11	Meiring 2007
Q1010-0047	1.3270	19.81 ± .05	12.46 ± 0.02	15.02 ± 0.02	<11.69	<12.37	Meiring 2007
Q1224+0037	1.2346	20.88 ± .05	12.34 ± 0.04	15.10 ± 0.07	<11.89	13.12 ± .09	Meiring 2007
Q1224+0037	1.2665	20.00 ± .07	12.00 ± 0.10	<14.30	<11.85	<12.37	Meiring 2007
Q2331+0038	1.1414	20.00 ± .05	12.48 ± 0.05	<14.33	12.12 ± 0.11	<12.37	Meiring 2007
Q0933+733	1.4790	21.62 ± .08	<12.75	15.52 ± .03	12.67 ± .14	13.46 ± .09	Khare 2004
SDSS J1028-0100	0.6321	19.9 ± .15	12.8 ± .24	15.28	12.46 ± .21	13.34 ± .13	Khare 2004
SDSS J1028-0100	0.7088	20.01 ± .15	13.13 ± .18	14.81	12.22 ± .76	13.23 ± .10	Khare 2004
SDSS J172+5302	0.9449	21.16 ± .13	12.9 ± .25	15.94 ± .02	13.27 ± .05	13.85 ± .02	Khare 2004
SDSS J172+5302	1.0311	21.61 ± .13	12.45 ± .02	15.60 ± .03	12.65 ± .05	13.39 ± .03	Khare 2004
SDSS J2340-0053	1.3606	21.63	12.83 ± .13	15.70 ± .02	12.62 ± .04	13.20 ± .04	Khare 2004
HE 1104-1805 A	1.6616	20.85 ± .01	12.41 ± .09	15.38 ± .02	12.48 ± .01	13.07 ± .01	Lopez 1999
Q0138-0005	0.7821	19.81 ± .09	12.66 ± .01	<14.89	12.69 ± .05	<12.61	Peroux 2002
Q0153+0009	0.7714	19.70 ± .09	12.88 ± .01	<14.49	<11.96	12.81 ± .10	Peroux 2002
Q0449-1645	1.0072	20.98 ± .07	12.37 ± .01	15.86 ± .03	12.62 ± .07	13.47 ± .02	Peroux 2002
PKS 0528-250	2.8112	21.35 ± .10	<12.8	16.00 ± .04	13.09 ± .07	13.65 ± .12	Srianand 1998
Q0240-2309	1.6718	19.79 ± .05	12.66 ± .03	14.95 ± .02	11.83 ± .03		Meiring 2010
Q0012-0122	1.3862	20.26 ± .02	11.73 ± .03	14.43 ± .08	<11.55	<11.89	Meiring 2009A
Q0021+0104A	1.3259	20.04 ± .11	12.16 ± .04	14.90	<11.48	<12.21	Meiring 2009A
Q0021+0104B	1.5756	20.48 ± .15	12.61 ± .03	14.88 ± .03	<11.95	<12.58	Meiring 2009A
Q2051+1950	1.1157	20.00 ± .15	12.64 ± .02	15.15 ± .07	12.90 ± .1	12.89 ± .10	Meiring 2009A
Q2352-0028B	1.0318	19.18 ± .13	12.53 ± .02	15.49 ± .03	<11.93	12.96 ± .06	Meiring 2009A
J1237+0647	2.6896	20.00 ± .15	13.03 ± .02	14.04 ± .09	12.75 ± .02		Noterdaeme 2010

**Table 4: Column Densities obtained from the literature. Although two objects are missing Cr II abundances, those values were not used in the correlation test.**



## Profile Fitting of Archival Spectra

The remaining six objects did not have published Mg I column densities, therefore we measured them using profile fitting software. While the H I, Si II, and Zn II abundances for these objects were all published either in Prochaska & Wolfe (1999) or Prochaska et al. (2007), the Mg I abundance was omitted. Their group has made all of these spectra (and many more) available in an online archive<sup>6</sup>, which is where we obtained them. These six were chosen from a set of 25 spectra which upon inspection, revealed the reasons for omitting Mg I due to a break in wavelength coverage, an inadequate signal-to-noise ratio, or blending with absorption from another system that made a clear measurement indiscernible. However, for six of these objects we were able to fit and obtain an Mg I column density: FJ0812+32, PH957 (Q0100+13), Q0841+12, Q1215+33, Q1331+17, and Q2231-00.

The software we used to do profile fitting is entitled FITS6P (Welty et al. 1997), written and maintained by Dan Welty with contribution from others<sup>7</sup>. FITS6P uses an iterative, least-squares procedure to fit a Voigt profile to specified absorption lines. Once specifications of the instrument and redshift of the absorber are entered, the user supplies test values of the parameters  $N$  (column density),  $b$  (Doppler parameter), and  $v$  (velocity). These may be individually varied or fixed as the fit is performed.

In general, we used the following procedure to obtain column densities for these objects. First, we isolated the region of the spectrum that contains the (rest frame) lines

---

<sup>6</sup> <http://msc.caltech.edu/archives/koa>

<sup>7</sup> <https://netfiles.uiuc.edu/dwelty/www/soft.html>

$\lambda\lambda\lambda 2056.5, 2062.5, 2066.4$  Cr II and  $\lambda 2062.9$  Zn II. These lines were then simultaneously fit to obtain  $N(\text{Cr II})$ ,  $N(\text{Zn II})$ ,  $b$ , and  $v$ . Then, in a separate run, we inserted these column densities as starting values to fit the  $\lambda 2026.4$  Cr II,  $\lambda 2026.6$  Zn II, and  $\lambda 2026.8$  Mg I lines. This method, although seemingly repetitive, is necessary to obtain the appropriate contributions from each ion in the blended line.

Figures 9-14 show our fits of these spectra. Table 5 shows the results of these measurements along with their  $1\sigma$  uncertainties also calculated by FITS6P.

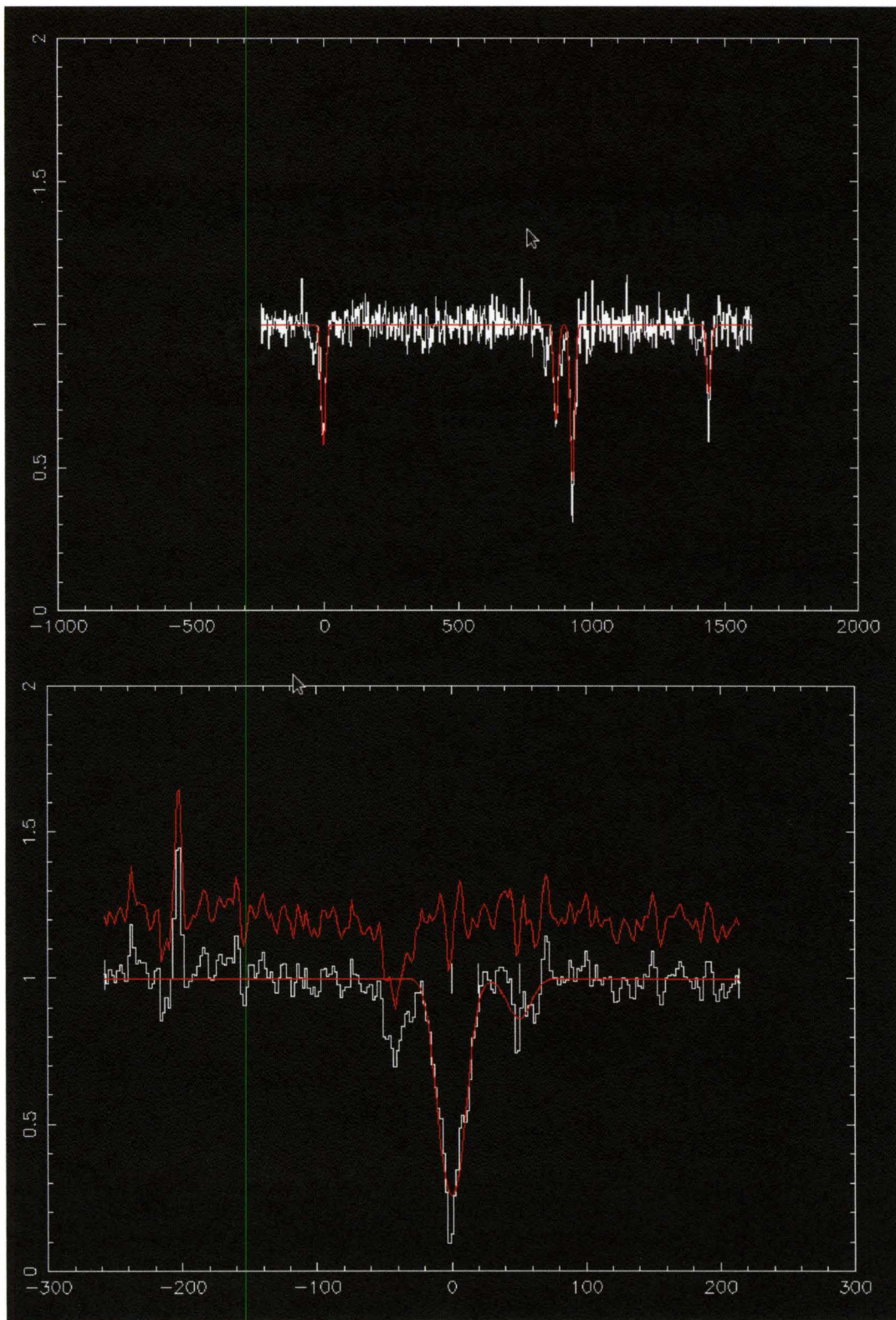


Figure 9: Absorption line profile fitting for FJ0812+32. The top figure represents fitting of the Cr II 2056, Cr II 2062, Zn II 2062, and Cr II 2066 lines, velocity centered on the Cr II 2056 line, while the bottom depicts fitting of the Zn II 2026, Cr II 2026, and Mg I 2026 lines, velocity centered on the Zn II line. This system has a redshift of 2.6263.

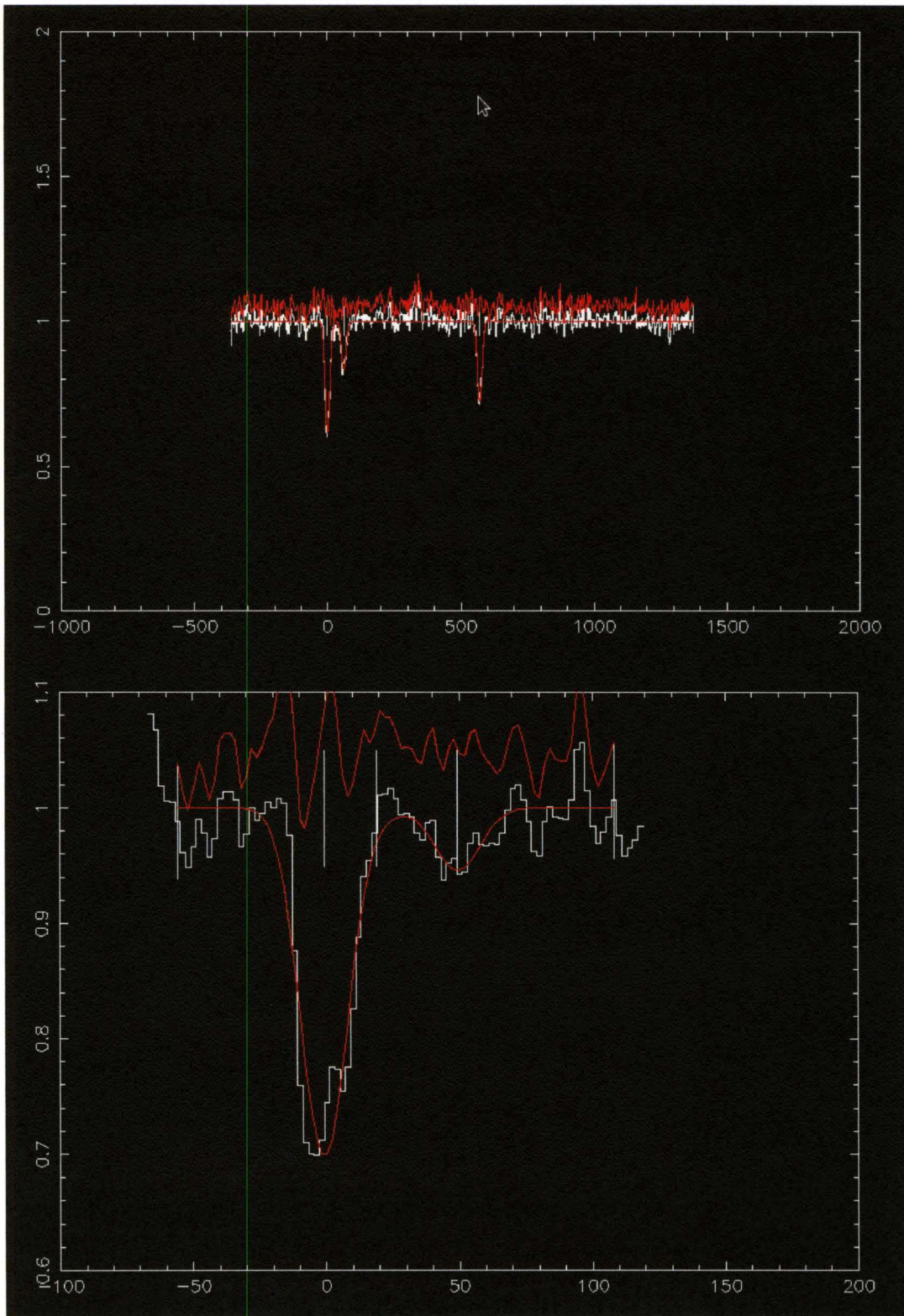
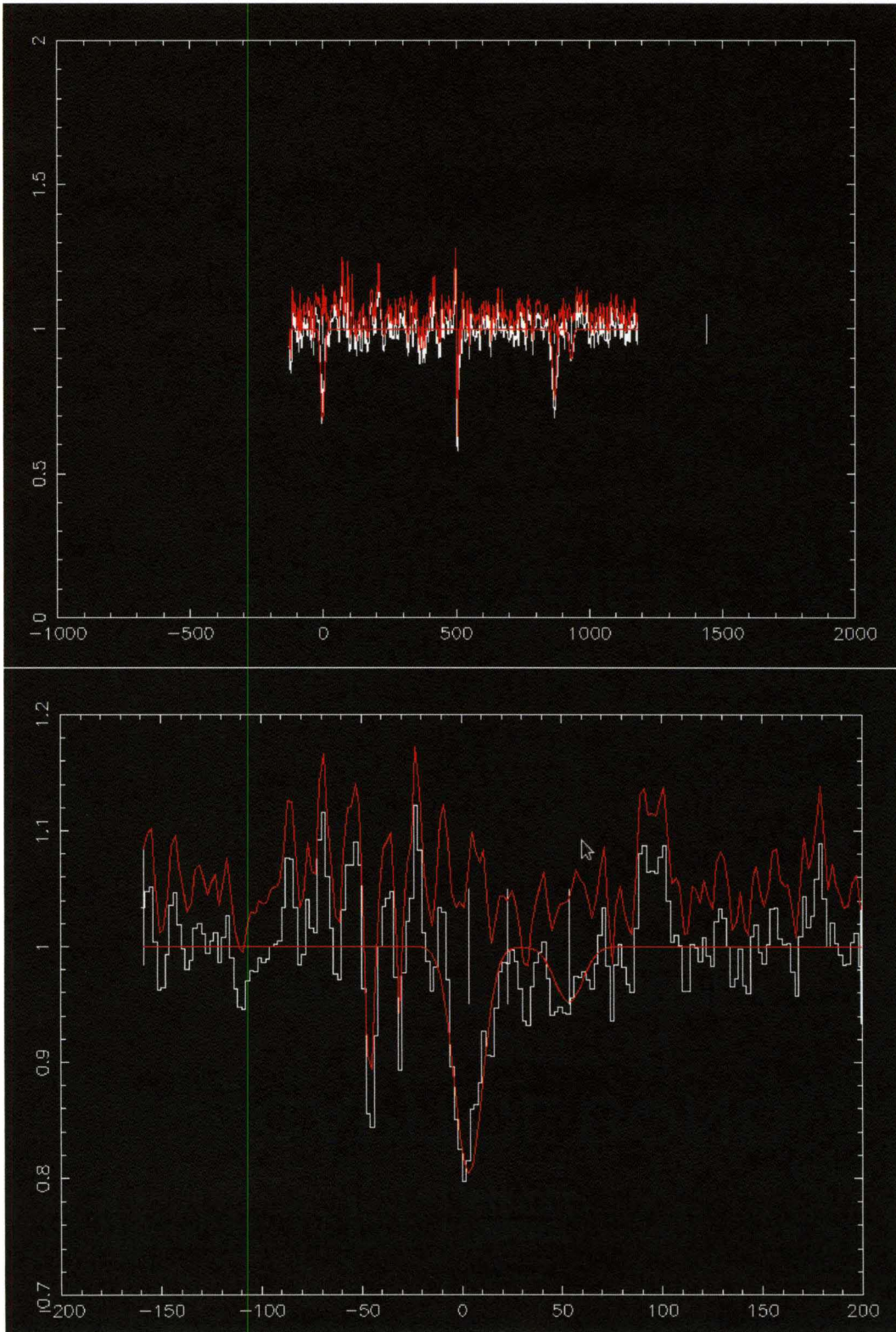
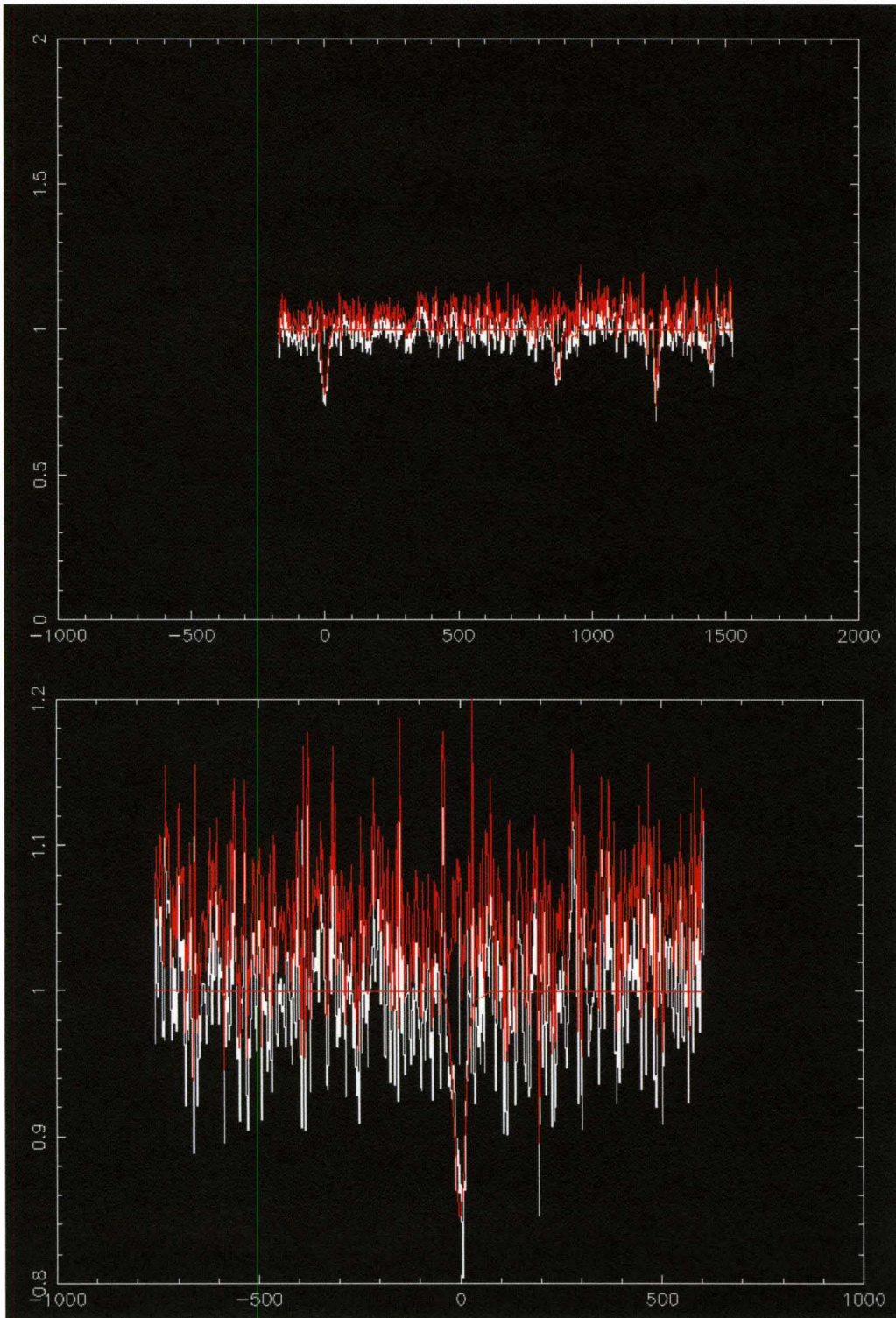


Figure 10: Absorption line profile fitting for PH957. The top figure represents fitting of the Cr II 2056, Cr II 2062, Zn II 2062, and Cr II 2066 lines, velocity centered on the Cr II 2056 line, while the bottom depicts fitting of the Zn II 2026, Cr II 2026, and Mg I 2026 lines, velocity centered on the Zn II line. This system has a redshift of 2.3090.



**Figure 11: Absorption line profile fitting for Q0841. The top figure represents fitting of the Cr II 2056, Cr II 2062, Zn II 2062, and Cr II 2066 lines, velocity centered on the Cr II 2056 line, while the bottom depicts fitting of the Zn II 2026, Cr II 2026, and Mg I 2026 lines, velocity centered on the Zn II line. This system has a redshift of 2.3750.**



**Figure 12: Absorption line profile fitting for Q1215. The top figure represents fitting of the Cr II 2056, Cr II 2062, Zn II 2062, and Cr II 2066 lines, velocity centered on the Cr II 2056 line, while the bottom depicts fitting of the Zn II 2026, Cr II 2026, and Mg I 2026 lines, velocity centered on the Zn II line. This system has a redshift of 1.999.**

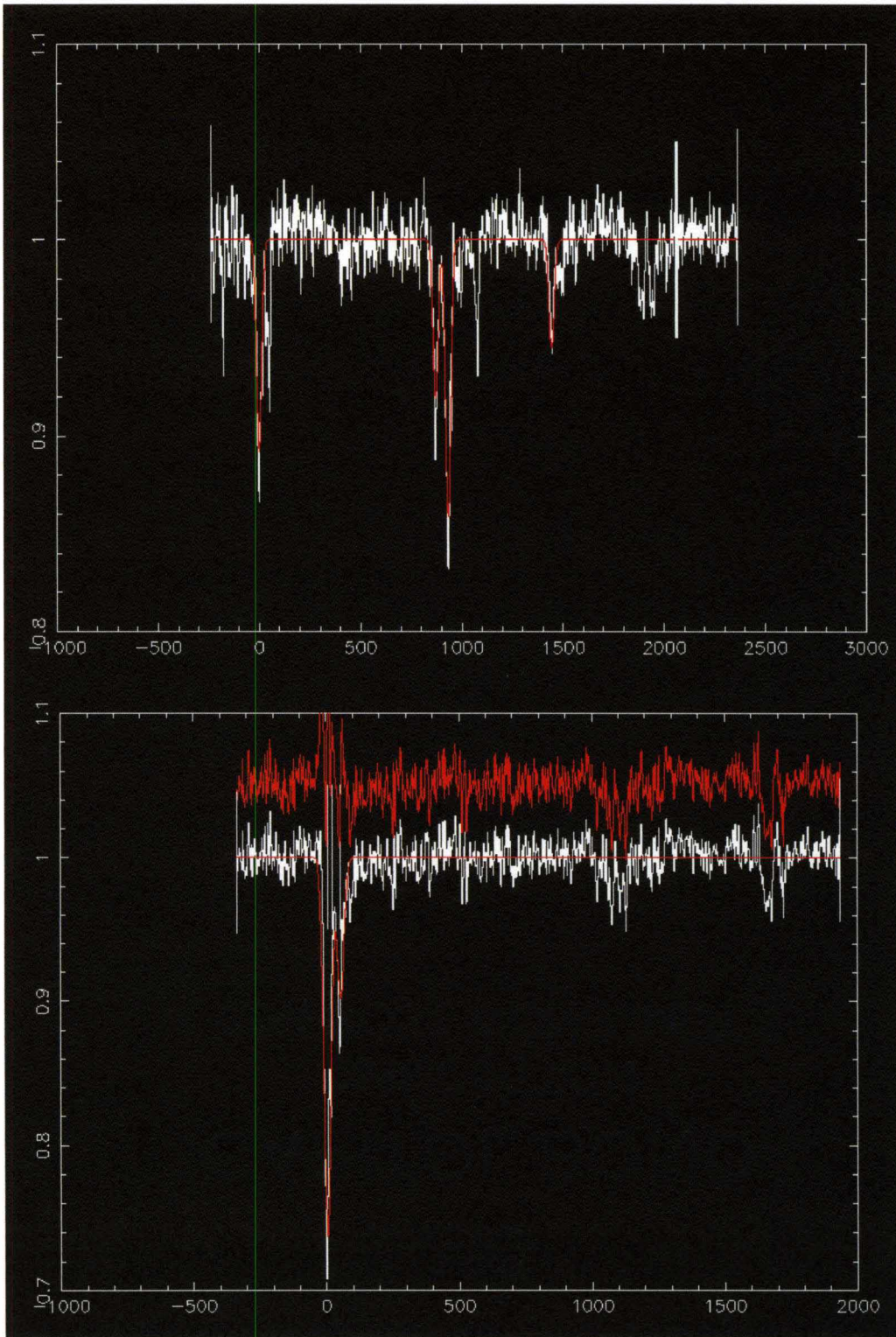


**Figure 13: Absorption line profile fitting for Q1331. The top figure represents fitting of the Cr II 2056, Cr II 2062, Zn II 2062, and Cr II 2066 lines, velocity centered on the Cr II 2056 line, while the bottom depicts fitting of the Zn II 2026, Cr II 2026, and Mg I 2026 lines, velocity centered on the Zn II line. This system has a redshift of 2.1.776.**

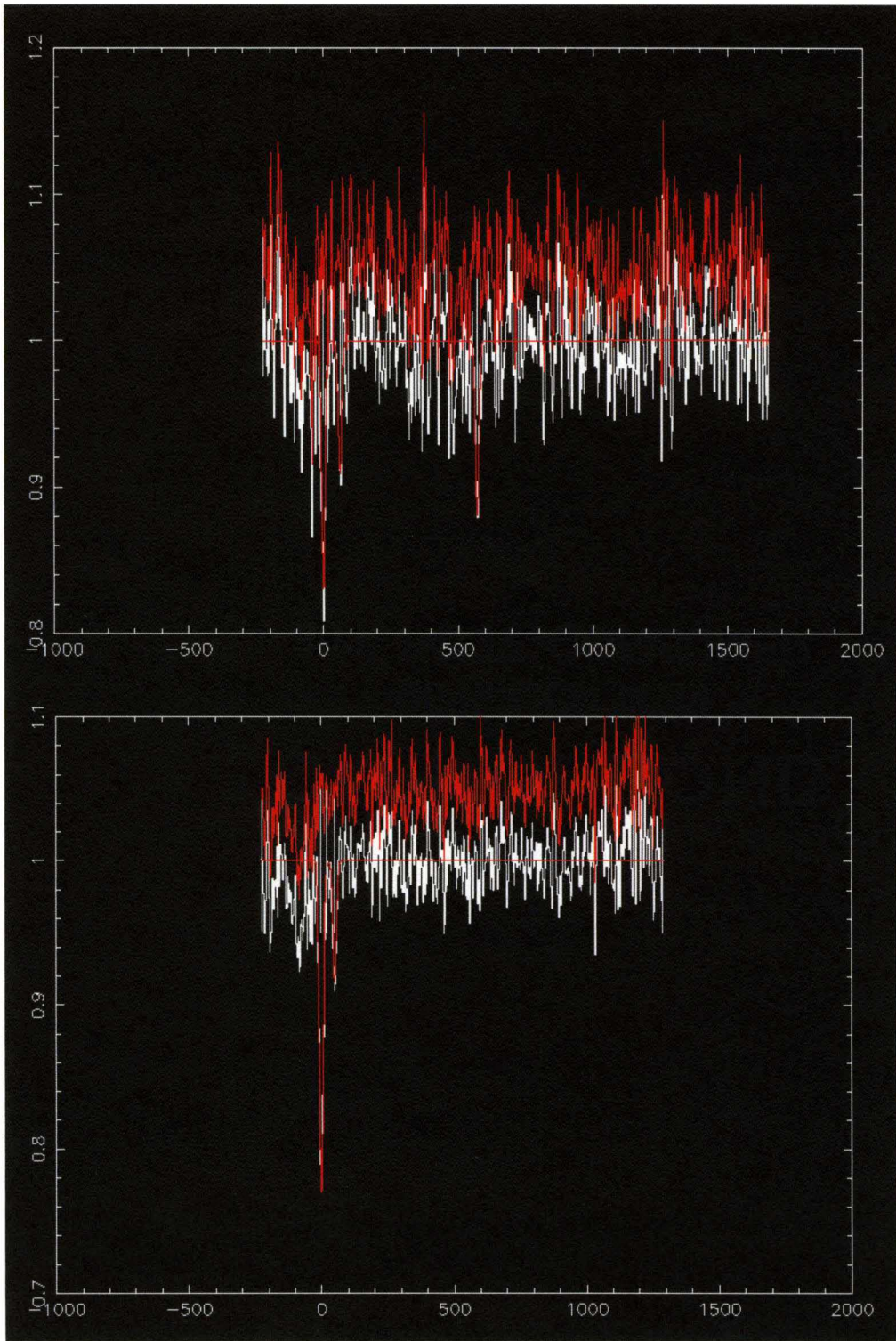


Figure 14: Absorption line profile fitting for Q2231. The top figure represents fitting of the Cr II 2056, Cr II 2062, Zn II 2062, and Cr II 2066 lines, velocity centered on the Cr II 2056 line, while the bottom depicts fitting of the Zn II 2026, Cr II 2026, and Mg I 2026 lines, velocity centered on the Zn II line. This system has a redshift of 2.066.



QSO	$z$	H I	Mg I	Si II	Zn II	Cr II	Paper
FJ0812+32	2.6263	$21.35 \pm .10$	12.71	$15.98 \pm .05$	13.04	$13.36 \pm .03$	Prochaska 2007
PH957(Q0100+13)	2.3090	$21.40 \pm .05$	12.284	>14.722	12.449	$13.387 \pm .015$	Prochaska 1999
Q0841+12	2.3750	$20.95 \pm .087$	12.26	$15.239 \pm .024$	12.15	$13.079 \pm .027$	Prochaska 1999
Q1215+33	1.9990	$20.950 \pm .067$	11.43	15.03	12.32	13.056	Prochaska 1999
Q1331+17	1.7760	$21.176 \pm .04$	12.74	15.285	12.57	12.82	Prochaska 1999
Q2231-00	2.0660	$20.560 \pm .10$	12.39	$15.247 \pm .019$	12.22	12.88	Prochaska 1999

**Table 5: Column Densities obtained from the profile fitting. H I column densities were available in the literature but others available in the literature were omitted in favor of the results from our profile fitting.**

## SECTION IV

### DATA ANALYSIS

To further explore the correlation between [Si II / Mg I] and [Zn II / H I], we used statistical analysis software routines that are a part of the Space Telescope Science Data Analysis System (STSDAS)<sup>8</sup>. The STSDAS package, developed at the Space Telescope Science Institute, is part of a larger system developed by the National Optical Astronomical Observatory called the Image Reduction and Analysis Facility (IRAF). The two routines used to analyze the data, `bhkmeth` and `schmittbin`, are discussed below.

#### **Kendall Tau Rank Correlation Coefficient**

In order to test whether or not these data are statistically correlated, we use the `bhkmeth` routine in IRAF to calculate the Kendall Tau Rank Correlation Coefficient. The Kendall Tau is generally calculated via a method by which simple comparison is performed on the pairs of data and the pairs are categorized as either *concordant* or

---

<sup>8</sup> [http://www.stsci.edu/resources/software\\_hardware/stsdas](http://www.stsci.edu/resources/software_hardware/stsdas) (Retrieved 4/6/2011)

*discordant* (Nelson 2001<sup>9</sup>). A pair is considered concordant if, given pairs  $(x_i, y_i)$  and  $(x_j, y_j)$ :

$$x_i < x_j \text{ and } y_i < y_j \quad \text{or} \quad x_i > x_j \text{ and } y_i > y_j$$

Conversely, a pair is said to be discordant if either of the following are true:

$$x_i < x_j \text{ and } y_i > y_j \quad \text{or} \quad x_i > x_j \text{ and } y_i < y_j$$

Let  $c$  equal the number of concordant pairs and  $d$  equal the number of discordant pairs.

The Kendall Tau is then defined as:

$$\tau = \frac{c - d}{c + d}$$

However, by the nature of these observations our data include upper limits and lower limits as well as detections. Therefore, we must use techniques referred to as *survival analysis* to account for this. The algorithms used in the STSDAS package employ survival analysis to handle *censoring*<sup>10</sup> of data, taking into account lower limits (right censored), upper limits (left censored), and detections.

The method by which IRAF calculates the Kendall Tau coefficient, established by Brown, Hollander, and Korwar (1974), is slightly modified from that described above. Much detail about this procedure is described by Isobe, Feigelson, and Nelson (1986), including a sample calculation. Here, the coefficient for a data set of  $n$  points is defined as:

---

<sup>9</sup> <http://eom.springer.de/K/k130020.htm> (Retrieved 4/6/2011)

<sup>10</sup> <http://stsdas.stsci.edu/cgi-bin/gethelp.cgi?censor> (Retrieved 4/6/2011)

$$\tau = \sum_{i=1}^n \sum_{j=1}^n a_{ij} b_{ij}$$

Where  $a_{ij}$  is equal to: 1 if  $x_i$  is definitely less than  $x_j$ , -1 if  $x_i$  is definitely greater than  $x_j$ , and 0 if the two are equal or if the comparison is uncertain.

Table 6 shows the data input into IRAF, including censoring flags. In cases where an upper limit was given for Mg I, the censoring reflects a lower limit since the calculation of [Si II / Mg I] places this in the denominator. The specification of the censoring flags is given in Table 3.

QSO	[Si/Mg]	[Zn/H]	Flag
Q0826-2230	2.13	0.68	-1
Q1009-0026	1.85	0.25	-1
Q1010-0047	2.56	-0.75	-2
Q1224+0037	2.76	-1.62	-2
Q1224+0037	2.3	-0.78	-3
Q2331+0038	1.85	-0.51	-1
Q0933+733	2.77	-1.58	1
SDSS J1028-0100	2.48	-0.07	0
SDSS J1028-0100	1.68	-0.42	0
SDSS J172+5302	3.04	-0.52	0
SDSS J172+5302	3.15	-1.59	0
SDSS J2340-0053	2.87	-1.64	0
HE 1104-1805 A	2.97	-1	0
Q0138-0005	2.23	0.25	-1
Q0153+0009	1.61	-0.37	-3
Q0449-1645	3.49	-0.99	0
PKS 0528-250	3.2	-0.89	1
Q0240-2309	2.29	-0.59	0
Q0012-0122	2.7	-1.34	0
Q0021+0104A	2.74	-1.19	4
Q0021+0104B	2.27	-1.16	-2
Q2051+1950	2.51	0.27	0
Q2352-0028B	2.96	0.12	-2
FJ0812+32	3.27	-0.94	0
PH957(Q0100+13)	2.438	-1.58	1
Q0841+12	2.979	-1.43	1
J1237+0647	1.01	0.34	0
Q1215+33	3.6	-1.26	0
Q1331+17	2.5412	-1.2364	0
Q2231-00	2.857	-0.97	0

**Table 6: Input table for survival analysis indicating censoring.**

Indicator	Independent variable	Dependent variable
0	detection	detection
1	detection	lower limit
-1	detection	upper limit
2	lower limit	detection
-2	upper limit	detection
3	lower limit	lower limit
-3	upper limit	upper limit
4	upper limit	lower limit
-4	lower limit	upper limit

**Table 7: Data censoring specification for the STSDAS survival analysis routines.**

The `bhkmetho`d routine outputs not only the Kendall Tau coefficient, but also a probability that a correlation does not exist (it assumes the null hypothesis). From our data, we calculate a Kendall Tau coefficient of -0.6115 and a 0.3% probability that a correlation does not exist.

### **Schmitt's Binned Linear Regression**

To attempt a linear fit to our data, we used the `schmittbin` routine (also a part of the IRAF/STSDAS package). The mathematical procedure for this linear regression is given by Schmitt (1985). Here we merely state the result of the calculation. The result is a slope of  $-0.5427 \pm 0.1249$  and an intercept of  $2.1432 \pm 0.1524$ . Figure 15 shows our data points overplotted with the result of this regression.

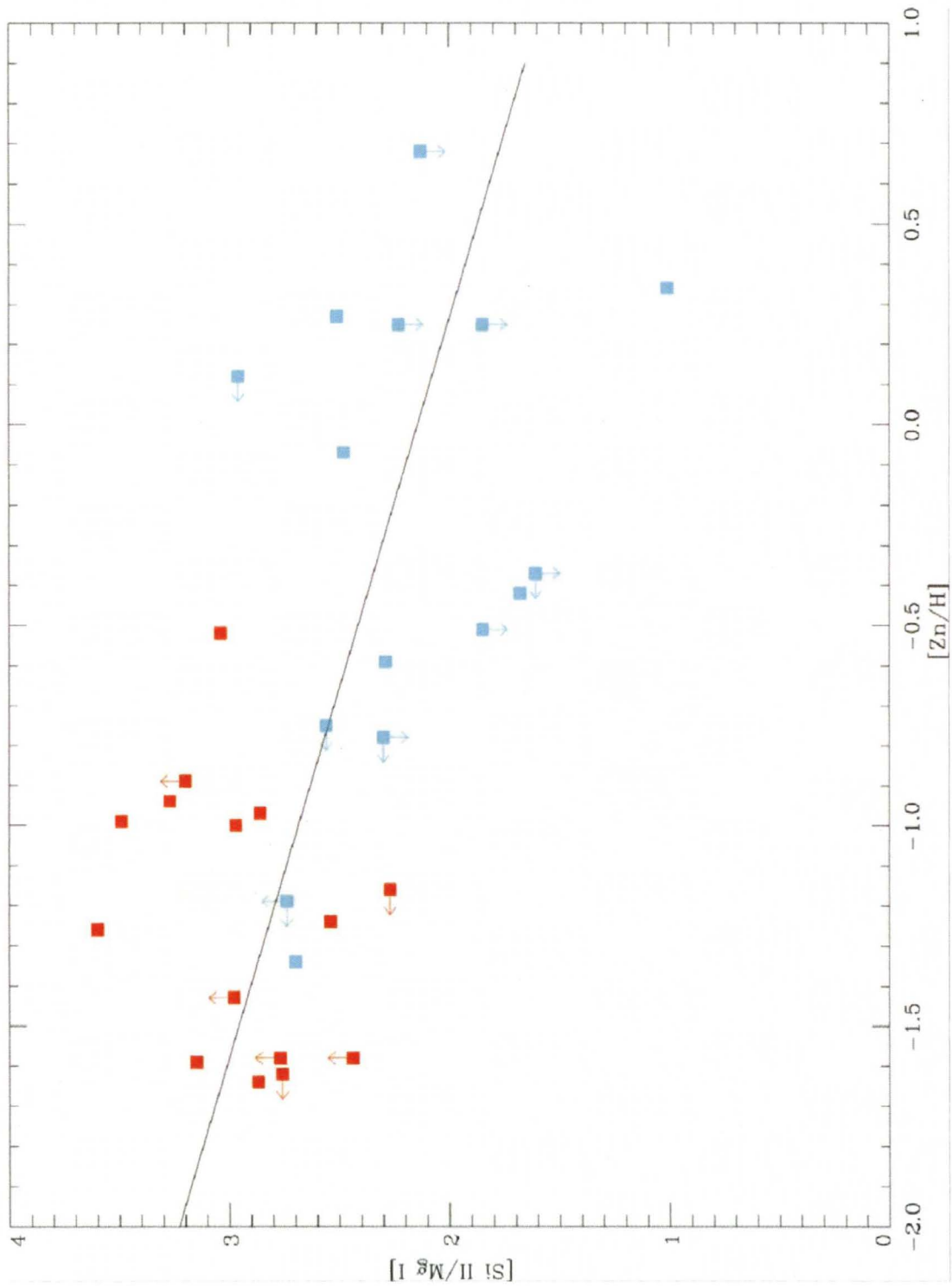


Figure 15: Plot of data sample with linear regression fit. Here, the red points indicate DLAs and blue points indicate Sub-DLAs.

## SECTION IV

### INTERPRETATION AND CONCLUSION

Statistically, the correlation we have measured between [Si II / Mg I] and [Zn II / H I] is quite convincing. However, the physical reasons giving rise to this correlation deserve investigation and in this section we present ensuing methods and possible scenarios responsible for this effect.

#### **Photoionization Models**

In an attempt to identify the physical conditions in DLAs and Sub-DLAs that result in the abundance ratio correlation, we ran several simulations of intergalactic gas clouds using the photoionization modeling software Cloudy<sup>11</sup>. Figure 16 shows the result of a large simulation where we attempted to recreate the observed trend. Here, a grid of calculations were performed varying H I column density from 18.5 – 21.5 and metallicity from -2 to 1 (both sets of quantities in logarithmic scale).

---

<sup>11</sup> Calculations were performed with version 08 of Cloudy, last described by Ferland et al. (1998).



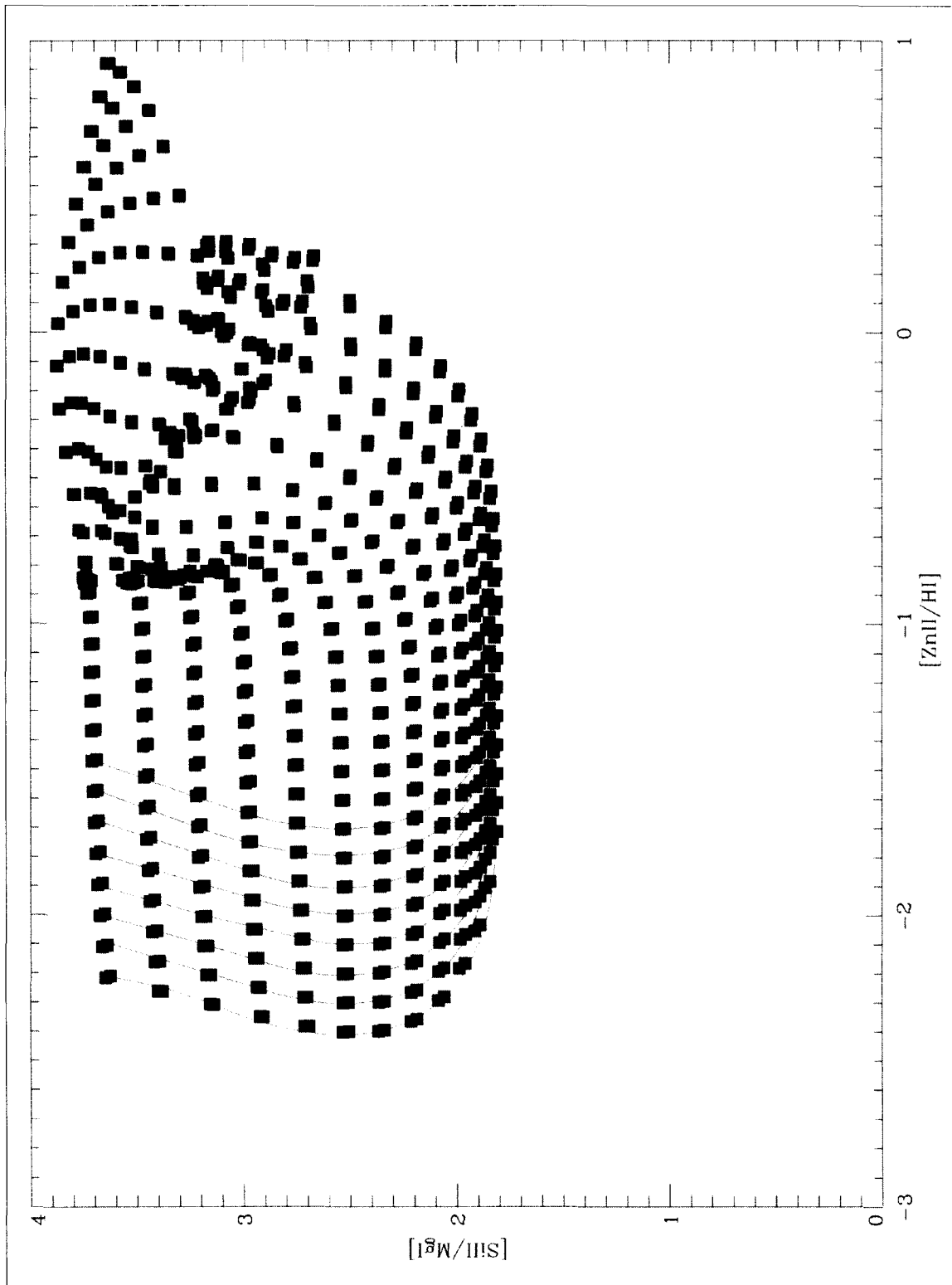


Figure 16: Results of Cloudy photoionization model calculations that were completed using input values of  $N(HI)$  spanning from 18.5 to 21.5 and a range of metallicity values reflecting the range of our sample. Curves of constant metallicity are shown here connecting several points.

While a correlation does not clearly emerge as observed from our sample, this brought about some interesting questions regarding Cloudy's treatment of certain physical parameters such as dielectronic recombination. As stated by de Boer et al. (1985), recombination increases sharply for Mg at ~5000 K. The question here was whether or not Cloudy was taking into effect this temperature dependence and thus impacting the calculated abundances of magnesium and silicon. A conference with Gary Ferland, Cloudy's author, confirmed that temperature dependence was incorporated into the software.

### **Dust Shielding**

Another possible cause of increased Mg I relative abundance with increasing metallicity is the presence of dust grains which shield ionizing photons. We may derive an estimated quantity of total dust grains by the following procedure. Since iron is generally heavily depleted, the abundance ratio [Fe / Zn] gives a measure of fraction of iron that remains in the gas phase. Therefore, the fraction settled onto dust grains should be given by one minus this quantity. We then add the relative abundance [Zn / H] and N(HI) to arrive the total column of Fe. Then the estimated number of grains should be:

$$\text{grains} \propto 10^{(1 - [\text{Fe} / \text{Zn}] + [\text{Zn} / \text{H}] + N[\text{HI}])}$$

We plot this quantity versus [Si II / Mg I] in figure 16.

## Dust Grains vs. [Si II / Mg I]

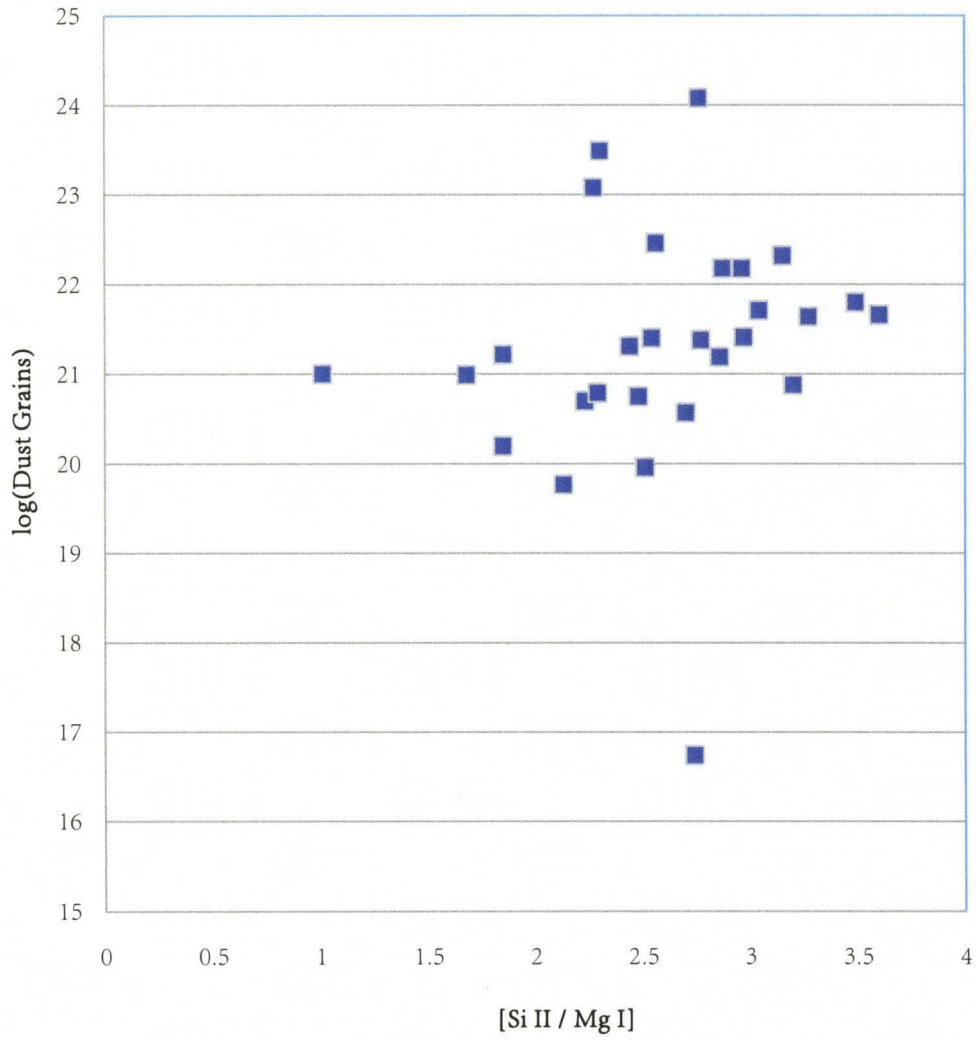


Figure 17: Dust depletion (as measured by the [Cr / Zn] ratio) plotted against [Si II / Mg I].

Upon running the same Kendall Tau correlation procedure outlined above on this relationship, we found a result of  $\tau = 0.4494$  which corresponds to a 3.08% probability that a correlation does not exist. Therefore, we are led to believe that dust shielding does play a role in the fact the higher metal-content (and higher dust-content) systems tend to exhibit more neutral magnesium.

### **Neutral Hydrogen Dependence**

Lastly, we consider the relationship between H I column density and metallicity. We stated in Section 2 that Sub-DLAs are more likely to be metal rich than DLAs therefore our correlation between metallicity and [Si II / Mg I] could be biased because of the dearth of metal-rich DLAs and metal-poor Sub-DLAs discovered thus far. Figure 18 shows a three-dimensional plot where the “z-axis” is  $N(H I)$ , indicating a decreasing metallicity with increasing neutral hydrogen.

Why would Sub-DLAs contain more Mg I? The answer may lie in the lesser amount of neutral gas within the system, thus greater ionization of the present hydrogen. With increased ionization overall, this would correspond to an increasing free electron density and increased likelihood of recombination. Isolating this free electron density as well as temperature (to account for the dielectronic recombination effect mentioned above) would prove necessary in the modeling process to recreate this trend.

Lastly, we conclude that more surveys of high column density absorbers will ultimately reveal the robustness of this trend. If metal poor Sub-DLAs are found to exist that do not exhibit this increasing neutral magnesium with increasing metallicity trend, it

will indicate a selection bias of metal-rich objects contributing to the perceived effect. Similarly, the discovery of metal-rich DLAs, possibly through increasingly blind surveys could also provide counterevidence. Objects observed until the present reveal few of these systems, although studies are taking place to examine potential selection effects. For instance, Fynbo et al. (2011) are looking at luminous galaxy counterparts to high column density absorbers and have discovered at least one metal rich system. As these types of observation programs are carried out, it will be particularly interesting to see if this reveals a plethora of metal-rich DLAs and where such metal rich DLAs exhibit increasing Mg I column density as do the Sub-DLAs.

## **Conclusion**

In this work, we have examined a correlation that seems to exist between  $[\text{Si II} / \text{Mg I}]$  and metallicity (as measured in  $[\text{Zn II} / \text{H I}]$ ) in DLAs and Sub-DLAs. Not only do we find that the correlation is statistically sound within our sample, but conclude that the presence of dust also contributes to increased neutral magnesium. However, the fact that known Sub-DLAs are relatively metal-rich as compared to DLAs may bias current samples as to enhance the effect seen here. As surveys continue to discover new and different high-column absorbers, usage of neutral magnesium as an easily measured proxy to trace the evolutionary history of metals in the gas and dust phase of the Universe will be further tested.

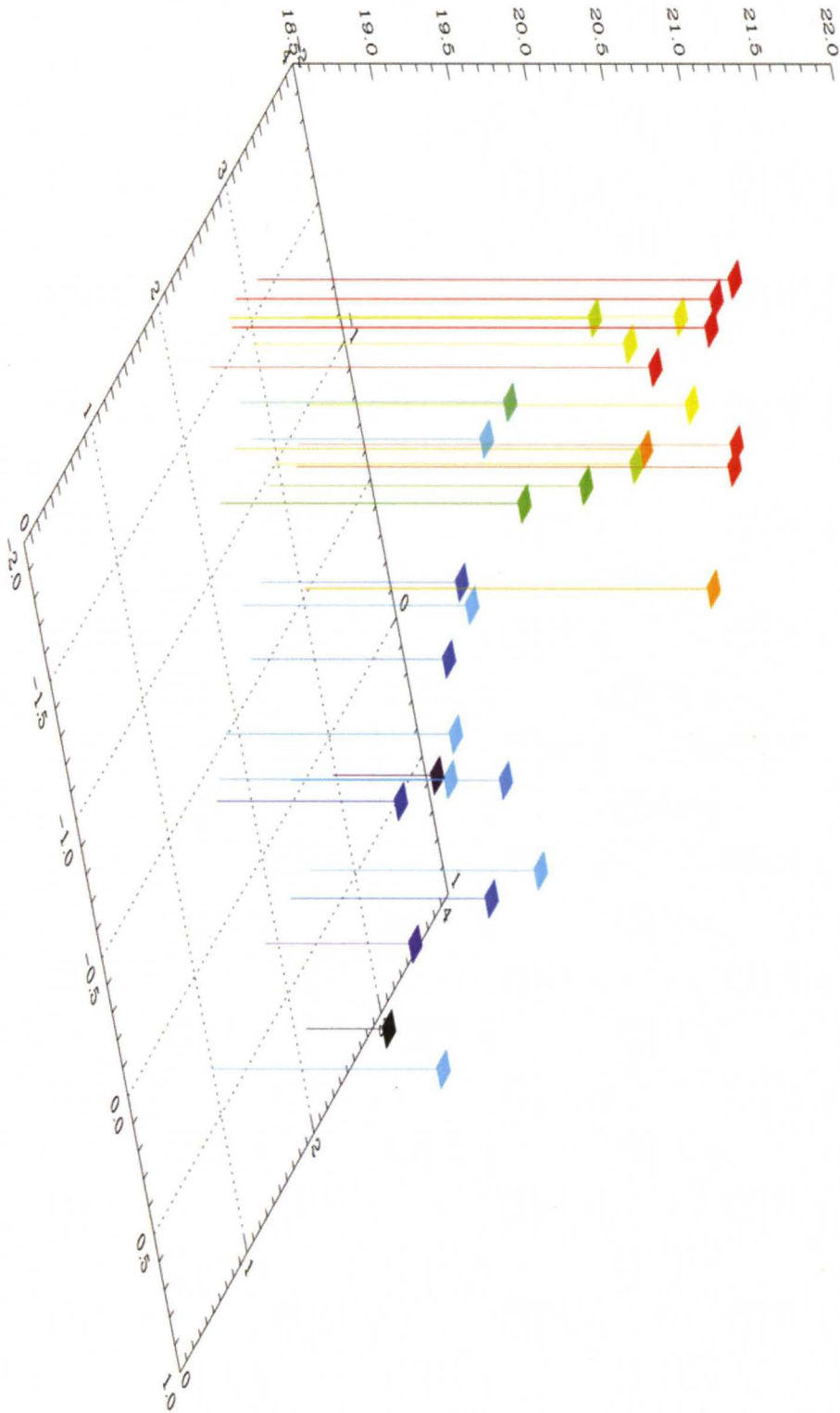


Figure 18: Similar to Figure 8, but the added dimension of neutral hydrogen column density. This plot

## REFERENCES

Brown, B.W.M., Hollander, M., and Korwar, R.M. 1974, Reliability and Biometry ed. F. Proschan and R.J. Serfling (Philadelphia:SIAM), p.327

de Boer, K. S.; Fitzpatrick, E. L. & Savage, B. D. (1985), 'Abundances of O, Mg, S, Cr, Mn, Ti, Ni and Zn from absorption lines of neutral gas in the Large Magellanic Cloud in front of R136', **217**, 115-126.

Carroll, B. W. & Ostlie, D. A. (2007), 'An Introduction to Modern Astrophysics'(15 April 2011).

Cartledge, S. I. B.; Clayton, G. C.; Gordon, K. D.; Bachford, B. L.; Sofia, U. J. & Wolff, M. J. (2006), FUSE Measurements of Extragalactic Interstellar Extinction, *in* & B.-G. Andersson G. Sonneborn, H. W. Moos, ed., 'Astrophysics in the Far Ultraviolet: Five Years of Discovery with FUSE', pp. 418-+.

Dyson, J. E. & Williams, D. A. ( 1980 ), *Physics of the interstellar medium / J.E. Dyson ; D.A. Williams* , Manchester University Press, Manchester : .

Ferland, G. J.; Korista, K. T.; Verner, D. A.; Ferguson, J. W.; Kingdon, J. B. & Verner, E. M. (1998), 'CLOUDY 90: Numerical Simulation of Plasmas and Their Spectra', **110**, 761-778.

Fynbo, J. P. U.; Laursen, P.; Ledoux, C.; Müller, P.; Durgapal, A. K.; Goldoni, P.; Gullberg, B.; Kaper, L.; Maund, J.; Noterdaeme, P.; Işstlin, G.; Strandet, M. L.; Toft, S.; Vreeswijk, P. M. & Zafar, T. (2010), 'Galaxy counterparts of metal-rich damped Ly- $\alpha$  absorbers - I. The case of the  $z = 2.35$  DLA towards Q2222-0946', **408**, 2128-2136.

Isobe, T.; Feigelson, E. D.; Akritas, M. G. & Babu, G. J. (1990), 'Linear regression in astronomy.', **364**, 104-113.

Jenkins, E. B. (2009), 'A Unified Representation of Gas-Phase Element Depletions in the Interstellar Medium', **700**, 1299-1348.

Khare, P.; Kulkarni, V. P.; Lauroesch, J. T.; York, D. G.; Crofts, A. P. S. & Nakamura, O. (2004), 'Metals and Dust in Intermediate-Redshift Damped Ly- $\alpha$  Galaxies', **616**, 86-109.

Lauroesch, J. T.; Truran, J. W.; Welty, D. E. & York, D. G. (1996), 'QSO Absorption

Line Systems and Early Chemical Evolution', **108**, 641-+.

Lopez, S.; Reimers, D.; Rauch, M.; Sargent, W. L. W. & Smette, A. (1999), 'First Comparison of Ionization and Metallicity in Two Lines of Sight toward HE 1104-1805 AB at  $z=1.66$ ', **513**, 598-618.

Meiring, J. D.; Kulkarni, V. P.; Lauroesch, J. T.; Péroux, C.; Khare, P. & York, D. G. (2009), 'New Magellan Inamori Kyocera Echelle Observations of  $z = 1.5$  sub-damped Lyman  $\alpha$  systems', **393**, 1513-1530.

Meiring, J. D.; Lauroesch, J. T.; Habertzettl, L.; Kulkarni, V. P.; Péroux, C.; Khare, P. & York, D. G. (2011), 'SOAR imaging of sub-damped Lyman  $\alpha$  systems at  $z = 1$ ', **410**, 2516-2525.

Meiring, J. D.; Lauroesch, J. T.; Kulkarni, V. P.; Péroux, C.; Khare, P. & York, D. G. (2009), 'A MIKE + UVES survey of sub-damped Lyman  $\alpha$  systems at  $z = 1.5$ ', **397**, 2037-2048.

Meiring, J. D.; Lauroesch, J. T.; Kulkarni, V. P.; Péroux, C.; Khare, P.; York, D. G. & Crofts, A. P. S. (2007), 'New abundance determinations in  $z = 1.5$  QSO absorbers: seven sub-DLAs and one DLA', **376**, 557-572.

Mshar, A. C.; Charlton, J. C.; Lynch, R. S.; Churchill, C. & Kim, T.-S. (2007), 'The Kinematic Evolution of Strong Mg II Absorbers', **669**, 135-157.

Noterdaeme, P.; Petitjean, P.; Ledoux, C.; López, S.; Srianand, R. & Vergani, S. D. (2010), 'A translucent interstellar cloud at  $z = 2.69$ . CO, H<sub>2</sub>, and HD in the line-of-sight to SDSS J123714.60+064759.5', **523**, A80+.

Noterdaeme, P.; Srianand, R. & Mohan, V. (2010), 'Quasars probing intermediate-redshift star-forming galaxies', **403**, 906-919.

Prochaska, J. X.; Gawiser, E.; Wolfe, A. M.; Castro, S. & Djorgovski, S. G. (2003), 'The Age-Metallicity Relation of the Universe in Neutral Gas: The First 100 Damped Ly- $\alpha$  Systems', **595**, L9-L12.

Prochaska, J. X.; Gawiser, E.; Wolfe, A. M.; Cooke, J. & Gelino, D. (2003), 'The ESI/Keck II Damped Ly- $\alpha$  Abundance Database', **147**, 227-264.

Prochaska, J. X. & Wolfe, A. M. (1999), 'Chemical Abundances of the Damped Ly- $\alpha$  Systems at  $z=1.5$ ', **121**, 369-415.

Prochaska, J. X.; Wolfe, A. M.; Howk, J. C.; Gawiser, E.; Burles, S. M. & Cooke, J. (2007), 'The UCSD/Keck Damped Ly- $\alpha$  Abundance Database: A Decade of High-Resolution Spectroscopy', **171**, 29-60.



Péroux, C.; Dessauges-Zavadsky, M.; Kim, T.; McMahon, R. G. & D'Odorico, S. (2002), 'Nature and Properties of sub-DLAs (absorbers with  $10^{19} \text{ N(HI)} \leq 2 * 10^{20} \text{ cm}^{-2}$ )', **281**, 543-544.

Péroux, C.; Petitjean, P.; Aracil, B. & Srianand, R. (2002), 'A new measurement of zinc metallicity in a DLA at  $z=3.35$ ', **7**, 577-586.

Schmitt, J. H. M. M. (1985), 'Statistical analysis of astronomical data containing upper bounds - General methods and examples drawn from X-ray astronomy', **293**, 178-191.

Spitzer, L. (1978), *Physical Processes in the Interstellar Medium*, New York Wiley-Interscience.

Srianand, R. & Petitjean, P. (1998), 'Molecules in the  $z_{\text{abs}} = 2.8112$  damped system toward PKS 0528-250', **335**, 33-40.

Storrie-Lombardi, L. J. & Wolfe, A. M. (2000), 'Surveys for  $z=3$  Damped Ly- $\alpha$  Absorption Systems: The Evolution of Neutral Gas', **543**, 552-576.

Timmes, F. X. (1996), Chemical Evolution of Galaxies, in S. S. Holt & G. Sonneborn, ed., 'Cosmic Abundances', pp. 298-+.

Welty, D. E.; Hobbs, L. M. & Kulkarni, V. P. (1994), 'A high-resolution survey of interstellar NA I D1 lines', **436**, 152-175.

Welty, D. E.; Lauroesch, J. T.; Blades, J. C.; Hobbs, L. M. & York, D. G. (1997), 'Interstellar Abundances in the Magellanic Clouds. I. GHRS Observations of the Small Magellanic Cloud Star SK 108', **489**, 672-+.

Wolfe, A. M. (1995), Evolution of the Gas and Metal Content of the Universe from  $z=5$  to the Present, in C. Heiles & P. R. Shapiro A. Ferrara, C. F. McKee, ed., 'The Physics of the Interstellar Medium and Intergalactic Medium', pp. 478-+.

Wolfe, A. M. (1999), Kinematics of Ionized and Neutral Gas in Damped Ly- $\alpha$  Systems, in A. J. Bunker & W. J. M. van Breugel, ed., 'The Hy-Redshift Universe: Galaxy Formation and Evolution at High Redshift', pp. 575-+.

Wolfe, A. M.; Gawiser, E. & Prochaska, J. X. (2005), 'Damped Ly- $\alpha$  Systems', **43**, 861-918.

## **CURRICULUM VITAE**

### **Education**

M.S. in Physics and Astronomy Expected graduation Spring

2011

Institution: University of Louisville

Thesis advisor: Dr. James T. Lauroesch

B.S. in Mathematics Spring 2005

Institution: University of Louisville

Concentration: Computational and Applied Mathematics

### **Current Research Areas**

Interstellar Medium, QSO Absorption Lines, Asteroseismology, Stellar Evolution

Interactive Multimedia Public Outreach

### **Computer Experience**

Astronomical: IDL, IRAF, Cloudy

Programming/scripting languages: C/C++, Visual Basic, Python, FORTRAN

Web-based development: XHTML, CSS, ASP.NET (C# and VB), Javascript, XSL

General: LaTeX, Linux OS, Extensive experience with Adobe Creative Suite Software

### **Grants**

NASA Space Science Student Ambassador (2010-2011)	\$2600
Graduate Student Council Travel Award (2010)	\$300
Graduate Research and Creative Activities Grant (2010)	\$500
Graduate Student Council Travel Award (2009)	\$300

### **Awards/Honors**

William Marshall Bullitt Award for the Best Student Paper in Astronomy/Astrophysics  
(UofL 2010) -

“Enhanced Public Outreach with Asteroseismology”

### **Observing Experience**

6 nights using the Bok Telescope (2.1m) – Kitt Peak National Observatory

Medium-band imaging of Clowes-Campusano Large Quasar Group

### **Academic Experience**

Graduate Teaching Assistant in Physics and Astronomy (U. of Louisville)

2009-Present

Position includes instruction of undergraduate laboratories and recitation sections

in general physics, kinematics and sound, electricity and magnetism, and general astronomy. Additional responsibilities include tutoring for all undergraduate physics courses as well as grading of exams and homework for large lecture sections.

Research Assistant (U. of Louisville)

2010

Projects have include investigating variability in time-separated QSO spectra (UVES) and ionization/metallicity correlation in Damped Lyman- $\alpha$  absorbers.

Author of Student Solutions Manual to *Modern Physics for Scientists and Engineers*

2010

This ancillary to the sophomore-level text in modern physics written by Dr. John C. Morrison and published by Elsevier includes descriptive, worked-out solutions to end-of-chapter problems.

Private Instrumental Music Instruction

2002-Present

I have professionally taught students of guitar, mandolin, and violin from all age groups and musical backgrounds.

### **Other Interests/Activities**

Founding board member of Star Duck Charities, a 501(c)(3) nonprofit organization dedicated to improving the lives of at-risk orphan children. Fundraising efforts have raised over \$50,000 for local youth.

Organizer of Astrolunch – our astronomy research group’s bi-weekly journal meeting.

**Affiliations**

American Astronomical Society

Society of Physics Students

**Publications**

“Ionization and Metallicity Correlation in Damped Ly- $\alpha$  Systems”

Burchett, J.; Lauroesch, J.; Meiring, J.; Kulkarni, V.; Khare, P.; York, D.; In preparation.

Instructor Solutions Manual for *Modern Physics for Scientists and Engineers*, Elsevier  
(2010).

Student Solutions Manual for *Modern Physics for Scientists and Engineers*, Elsevier  
(2010).